P-wave Reflectivity of the Crust and Upper Mantle Beneath the Southern Appalachians and Atlantic Coastal Plain using Global Phases

Devon N. Verellen[1], Erik C. Alberts[2], Gustavo A. Larramendi[3], E. Horry Parker, Jr.[4], and Robert B. Hawman[3]

[1]Chevron
[2]Exxon/Mobil
[3]University of Georgia
[4]Black & Veatch

November 21, 2022

Abstract

Reflection profiles generated using PKPdf as a virtual source show laterally continuous reflections from structures at depths less than 1 km to roughly 200 km beneath the southern Appalachian orogen and Atlantic Coastal Plain. Arrivals interpreted as reflections from the Moho increase in time from ~10 s beneath the Coastal Plain to 17.4 s (~57 km) beneath the Blue Ridge Mountains, providing additional evidence that the southern Appalachians are in rough isostatic equilibrium. Reflections at 32-36 s (120-135 km) are consistent with the depth to the base of the lithosphere found in recent inversions of Ps arrivals and surface waves. Alternatively, these and later reflections at times up to 58 s (~224 km) may be due to layering associated with drag-induced flow in the asthenosphere, suggesting largely horizontal rather than vertical flow for depths less than 225 km beneath the Georgia coastal plain.

P-wave Reflectivity of the Crust and Upper Mantle Beneath the Southern Appalachians and Atlantic Coastal Plain using Global Phases

Devon N. Verellen[1], Erik C. Alberts[2], Gustavo A. Larramendi, E. Horry Parker, Jr.[3], and Robert B. Hawman

Department of Geology, University of Georgia, Athens, GA, USA

[1]now at Chevron, Houston TX
[2]now at Exxon/Mobil, Houston, TX
[3]now at Black & Veatch, Greenville, SC

KEY POINTS

- P-wave reflections generated using PKPdf as a virtual source are observed over depths from 1 km to greater than 200 km.
- Reflection times reach 17.4 s (> 55 km) for the highest elevations, supporting previous evidence that the southern Appalachians are in isostatic equilibrium.
- Reflections at 32-36 s (120-135 km) may indicate drag-induced flow at the base of the lithosphere. These arrivals are observed for single as well as stacked events.

INDEX TERMS
- Seismology
- Tectonophysics

KEYWORDS
- southern Appalachians, Atlantic Coastal Plain, PKPdf, PKIKP, Moho, LAB

PLAIN LANGUAGE SUMMARY

The main goal of this work was to study the nature of the boundary between the tectonic plate beneath the southern Appalachians and the underlying, more fluid mantle. We used echo soundings to determine the depth and physical characteristics of major layers. Our strategy was to use seismic waves generated by earthquakes on the opposite side of the planet as an energy source. We see a major transition at depths of 120-135 km that we interpret as drag-induced flow just beneath the plate. We also see evidence for a thickening of Earth's crust beneath the highest elevations of the southern Appalachians that suggests that these very old mountains are in gravitational equilibrium.

Abstract

Reflection profiles generated using PKPdf as a virtual source show laterally continuous reflections from structures at depths less than 1 km to roughly 200 km beneath the southern Appalachian orogen and Atlantic Coastal Plain. Arrivals interpreted as reflections from the Moho increase in time from ~10 s beneath the Coastal Plain to 17.4 s (~57 km) beneath the Blue Ridge Mountains, providing additional evidence that the southern Appalachians are in rough isostatic equilibrium. Reflections at 32-36 s (120-135 km) are consistent with the depth to the base of the lithosphere found in recent inversions of Ps arrivals and surface waves. Alternatively, these and later reflections at times up to 58 s (~224 km) may be due to layering associated with drag-

induced flow in the asthenosphere, suggesting largely horizontal rather than vertical flow for depths less than 225 km beneath the Georgia coastal plain.

1. Introduction

The passage of USArray across the eastern United States has resulted in fundamentally new insights into the fine-scale structure of the continental lithosphere. Recent analyses of Transportable Array (TA) data for upper mantle structure, including body-wave and surface-wave tomography and analyses of shear-wave splitting, indicate that the lithosphere thins from a maximum of 200-250 km beneath the North American craton [*Yuan et al.,* 2014] to roughly 150 km beneath the Grenville Front and Appalachian Mountains (Valley & Ridge and Blue Ridge), to less than 100 km beneath portions of the SE Atlantic Coastal Plain [*Pollitz and Mooney,* 2016; *Shen and Ritzwoller,* 2016; *Savage et al.,* 2017]. Analyses of shear-wave splitting generally show fast axes parallel to absolute plate motion (APM) beneath the craton [*Yuan et al.,* 2014; *Long et al.,* 2016; *Yang et al.,* 2017] with more complex patterns eastward toward the continental margin.

These patterns have been interpreted using a variety of models. For instance, fast axes parallel to the belt of highest elevations in the Appalachian Orogen are also roughly parallel to APM; they have been interpreted both as evidence for strain associated with Alleghanian collision frozen into the lithosphere [*Long et al.,* 2016] and as simple shear generated just above and below the lithosphere-asthenosphere boundary (LAB) by ongoing plate motion [*Yang et al.,* 2017]. Beneath the southeastern U.S. coastal plain, interpretations of a broad zone of null [*Long et al.,* 2016] or small [*Yang et al.,* 2017] splitting times include vertical flow in the asthenosphere (possibly a consequence of edge-driven convection driven by an abrupt transition in lithospheric thickness) [*Long et al.,* 2016; *Savage et al.,* 2017] combined with weak or spatially incoherent anisotropy in the lithosphere. An alternative model involves cancellation of the effects of APM-parallel flow within the broad lithosphere-asthenosphere transition zone by roughly N-S directed flow in the asthenosphere diverted around the keel of the craton [*Yang et al.,* 2017].

Vertical incidence reflection profiling has the potential to help resolve some of these issues by tracking the lateral continuity of structures within the uppermost mantle. Several large-scale, active-source experiments across Eurasia have been able to detect coherent reflections at normal incidence in the mantle to depths greater than 200 km using large explosions [*Knapp et al.,* 1996; *Steer et al.,* 1998]. In this study, we use the global seismic phase PKIKP (PKPdf) as a virtual source [*Ruigrok and Wapenaar,* 2012] to construct normal-incidence reflection sections that are analogous to those produced by active-source reflection profiling of the crust. The strategy for this work is to take advantage of the relatively dense station spacing of the broadband arrays deployed during the Southeastern Suture of the Appalachian Margin experiment (SESAME) (Figure 1) [*Parker et al.,* 2013] to investigate P-wave reflectivity or "fabric" over a portion of the upper mantle for which the long-wavelength velocity and anisotropy structure are well constrained by recent analyses of TA data.

2. Geologic and Tectonic Setting

The southern Appalachians (Figure 1) are the product of diachronous, largely oblique collision of Laurentia with Gondwana and a number of continental fragments and island arcs [*Hatcher,* 1989, 2002, 2010; *Hatcher et al.,* 2007], beginning ~480 Ma and culminating in the Alleghanian orogeny (330-260 Ma). Detachment faults imaged by the Consortium for Continental Reflection Profiling (COCORP) indicate that late Alleghanian collision drove rocks of the Carolina terrane, Inner Piedmont, and Blue Ridge several hundred km to the northwest [*Cook and Vasudevan,* 2006; *Duff and Kellogg,* 2017].

Rifting of the orogen began in the late Triassic, followed by seafloor spreading and opening of the Atlantic by 180 Ma. Beneath Line E, rift basin sediments are restricted to the north end, where they are less than 2500 m thick, but are more extensive beneath Line W where they reach thicknesses of 1000-6000 m [*McBride,* 1991]. Subsequent variations in sea level are recorded in the Atlantic Coastal Plain of Georgia and Florida as a sequence of poorly consolidated Cretaceous and Cenozoic carbonates and siliciclastics up to 2000 m thick [*Chowns and Williams,* 1983].

3. Using PKPdf/PKiKP to image P-wave reflectivity

The method used in this study is a modification of an approach known as global phase seismic interferometry or "GloPSI" *[Ruigrok & Wapenaar,* 2012*]*. This approach uses PKIKP (referred to in the rest of this discussion as PKPdf) and PKiKP phases as virtual seismic sources for generating P-wave reflections from the crust and upper mantle. In contrast with other methods for seismic imaging such as receiver functions, GloPSI uses only the vertical component of ground motion. Upon reflection from the earth's surface, these phases reverse polarity and propagate downward as plane waves with near-vertical raypaths. Therefore they preferentially image structure with small dips.

3.1. Processing

Most previous analyses of PKPdf/PKiKP (e.g., *Ruigrok and Wapenaar,* 2012) have taken advantage of the equivalence of the P-wave reflection response (the wavefield recorded for a coincident source and receiver) to the positive lags of the autocorrelation of the transmission response (the wavefield recorded at the surface for a source below the depth range of interest) [*Claerbout,* 1968]. Unfortunately, in the absence of large numbers of earthquakes for stacking, the lags of the autocorrelation corresponding to the early part of the output section tend to be dominated by energy associated with the extended source wavelets.

We try a different approach based on deconvolution of traces prior to stacking using an estimate of the source wavelet for each earthquake. We combine traces from the three profiles (D, W, E) into a single gather and then align first (PKPdf) arrivals by cross correlation. This provides a common time base with the time of the deconvolved first arrival serving as the origin time of reflections. This approach is similar to the method employed by Langston and Hammer [2001] and Yang et al. [2012] for the analysis of teleseismic waves. Following those authors, we estimate source wavelets by stacking seismograms for stations deployed on bedrock, north of the Coastal Plain. The assumption is that lateral variations in structure lead to cancellation of reflections, leaving only the common source wavelet of the earthquake.

This approach can be complicated by the arrival of two phases (PKPdf and PKiKP) in the time window of interest. For a source depth of 100 km and distances of 115°-140°, travel times for the two phases differ by ~ 0-3 s and ray parameters differ by 0.01–0.26 s/°. Free-surface reflections (pPKPdf and pPKiKP) in the source region have ray parameters that are nearly identical to those for the corresponding arrivals PKPdf and PKiKP. For the earthquakes used in this study, the effective array apertures for stations deployed north of the Coastal Plain ranged from 1.7°–2.6° and the differential moveouts ranged from 0.1-0.4 s. The stacking procedure described above treats all these phases as a single arrival and therefore yields an effective source wavelet of extended duration, with some loss of resolution at higher frequencies. Differential moveouts for PKPdf and PKiKP between those stations and the southernmost stations range from 0.1-1.1 s; this causes some broadening of deconvolved waveforms that is minimized by stacking (Figures S8-S9).

Over the distance range 115°-145°, interference from PP, which follows PKPdf by 60 – 180 s, is largely avoided, but earthquakes in the distance range 145°-155° are not included in the analysis because of interference with the phases PKPab and PKPbc. Scattering by lateral heterogeneities near the base of the mantle can also contaminate the record [*Hedlin et al.,* 1997]; this situation is flagged by coherent energy arriving shortly before PKPdf. Beyond 160°, PKPdf and PKPab diverge rapidly, but the listening window is restricted by PKP_{diff}, the diffraction along the inner/outer core boundary, which follows PKPdf by 14-34 s.

3.2 Results

Deconvolution was carried out in the frequency domain. We used a water-level value of 0.0001 to stabilize spectral division and a range of Gaussian functions (α = 1.0 – 4.0) to smooth the output waveforms [Langston, 1979]. Deconvolved gathers for single earthquakes were stacked to suppress noise (both random and coherent) and to enhance signal levels. Prior to stacking, each trace was normalized by the amplitude of the direct PKPdf arrival, then divided by the RMS value of noise 0-18 s prior to PKPdf to give greater weight to seismograms with higher signal levels. After stacking, samples were multiplied by a factor equal to the square root of two-way time to smoothly increase amplitudes of later reflections.

The deconvolved direct arrival at time zero is assigned a positive polarity. As noted earlier, upon reflection at the earth's surface, this polarity is reversed. Therefore the direct arrival and reflections from positive impedance contrasts (e.g., crust over mantle) will show opposite polarities. The 16 earthquakes used in this study are summarized in Table S1. The resulting stacks (Figures 2-4 and S3-S6) show coherent reflections with dominant periods ranging from 1-4 s and from interfaces in the near surface to depths of ~200 km.

3.2.1. Coastal Plain Sediments

For stations over the Coastal Plain, vertical stacks and many of the records for individual events show a series of strong, coherent reflections 0.2-4.2 s after the direct arrival (Figures 2 and S4). Travel times for the peak of the first half cycle (0.2-1.4 s; opposite in polarity from PKPdf, indicating a positive impedance contrast) match those predicted for reflection from the base of the sequence of Cretaceous and younger sediments and poorly consolidated sedimentary rocks. This event starts very close to the feather edge of the sequence at the northern boundary of the Coastal Plain and increases in travel time to the south, in agreement with thicknesses derived from well data [Chowns and Williams, 1983]. For Line E (Figure S4), travel times are best fit by an average P-wave velocity of 2400 m/s for stations E31 to E25 and by a slightly greater average velocity (2600 m/s) for the thicker sequences beneath stations E24-E07. For Line W (Figure 2), the best fits are obtained for velocities of 2200 m/s for stations W21-W19, 2400 m/s for stations W18-W10, and 2100 m/s for stations W09–W01. These values are consistent with those reported by Iverson and Smithson [1983] and Barnes and Reston [1992].

Travel times for the later 2-3 half-cycles are consistent with times predicted for free-surface multiples. Travel times for the second multiple bounce overlap those predicted for the base of the underlying Triassic/Jurassic sedimentary sequence; resolution of the latter will require additional deconvolution (work in progress).

3.2.2. Moho

For Line W, events interpreted as Moho reflections are clearest at lower frequencies (α=1.0; Figure 2). Two-way times vary between 9.7 and 10.1 s for stations W02 to W06 and between 10.0 and 10.9 s for stations W07 and W22, all within the Coastal Plain. Moho reflection times reported for coincident COCORP lines [*McBride,* 1991] are somewhat greater (11.2 – 12.0 s), suggesting that the broader PKPdf-generated waveforms may represent a composite of reflections from lower crustal layering and the crust-mantle transition itself (work in progress). A similar result is obtained for Line E (Figure S3). From station W22 the times increase northward, from 12.2 s at station W23 to 12.8 s (crustal thickness: 42 km) at station W31 (Inner Piedmont), with a pronounced increase from 13.8 s (45 km) at W315 (foothills) to 17.4 s (57 km) beneath W35 in the Blue Ridge Mountains. A similar trend is observed for Line D (Figure S2). These are the first observations of normal-incidence P-wave reflections from the Moho beneath the higher elevations of the southern Appalachians. The results for Lines W and D are consistent with other broadband and active-source results suggesting that the southern Appalachians are in rough local isostatic equilibrium [*French et al.,* 2009; *Hawman et al.,* 2012; *Schmandt et al.,* 2015; *Parker et al.,* 2013; 2016; *Hopper et al.,* 2016].

3.2.3. Upper Mantle

Stacks for Line E show reflections at 16-20 s (depths: 50-75 km; Figures 3 and S4). A similar reflection sequence is not seen in the stacks for Line W, but reflections in this depth range do appear in sections derived by pre-stack migration (Figure S10; see below). Models of S-wave velocity for the southern Appalachian highlands, derived by inversion of surface waves [*Savage et al.,* 2017], show a low-velocity zone over a similar depth range. Similar "mid-lithospheric discontinuities" occur throughout the North American craton and are variously interpreted as low-velocity cumulate layers, refertilized depleted mantle, stacks of oceanic plates, and underplating [*Abt et al.,* 2010; *Calo et al.,* 2016]. Alternatively, the reflections could be generated by layers within the uppermost mantle depleted by partial melting during Mesozoic extension [*Pollitz & Mooney,* 2016].

For Lines E and W, multicyclic reflections between 32 s and 36 s are consistent with a layered zone at depths of 120 - 135 km (Figures 3, 4, S4, S5). This is roughly 30 km deeper than the lithosphere/asthenosphere boundary (LAB) inferred from analysis of Sp receiver functions for a nearby broadband station [*Abt et al.,* 2010] but is in better agreement with more recent studies based on inversion of surface waves [*Savage et al.,* 2017] and joint inversion of surface waves and Ps receiver functions [*Calo et al.,* 2016].

The frequency content and multicyclic character of the reflections indicates much smaller wavelength variations in velocity than expected for a purely thermal boundary. At these depths, quarter-wavelength estimates of vertical resolution, corresponding to layer thicknesses required for constructive interference of reflections from multiple layers, range from 3-8 km (Supplement). This scale of layering would be consistent with models incorporating the effects of shearing at the transition and also with intrusions triggered by partial melting of hydrated asthenosphere [*Fischer et al.,* 2010*; Till et al.,* 2010]. Alternatively, these and deeper signals at roughly 44 s (~167 km) and 58 s (~ 224 km) (Figure 4) may be reflections from layering associated with drag-induced flow in the asthenosphere [*Eaton et al.,* 2009*; Fischer et al.,* 2010*; Long et al.,* 2016]. The event at 58 s is close in depth to a transition identified beneath North America as the Lehmann discontinuity [*Calo et al.,* 2016]; this feature was originally interpreted as the base of a low-velocity zone [*Lehmann,* 1960] but could also represent an abrupt decrease in transverse anisotropy marking the base of a zone of strong coupling between asthenosphere and lithosphere [*Gaherty and Jordan,* 1995; *Eaton et al.,* 2009]. These deeper reflections are consistent with largely horizontal rather than vertical flow at depths less than 225 km beneath this portion of the Georgia Coastal Plain.

3.2.4. Individual Events

The above approach is capable of recovering useful signal levels for single earthquakes, even without stacking. Deconvolved records for individual events (Figure 5) show consistent results for earthquakes over a range of magnitudes and focal depths, indicating that major arrivals (particularly those interpreted as reflections from the LAB at 32-36 s) are indeed reflections and not artifacts generated by incomplete deconvolution of source-side scattering and other coherent noise (Figures S6 and S7).

However, the results for individual earthquakes do show some variations in arrival times and relative amplitudes for major arrivals, which tend to degrade the stacks (e.g., the events at 32-34 s in Figure 4), and also show variations in reflection density over different time windows. We attribute these variations to differences in dominant frequencies for different magnitude earthquakes, processing artifacts, particularly near the end of listening windows (Figure S6 and S7), small-scale lateral heterogeneity, and variations in back-azimuth. To define major structural boundaries, we rely on the stacked images. To preserve a composite image of finer-scale structure or “fabric”, we migrate the deconvolved sections for individual earthquakes separately and stack the results. Preliminary migration results based on a subset of events are presented in the Supporting Information (Figures S10 and S11).

4. Conclusions

Reflection profiles generated using PKPdf as a virtual seismic source show laterally continuous structures at depths from the near-surface to roughly 200 km beneath the southern Appalachian orogen and adjacent Atlantic Coastal Plain. Waveforms are deconvolved for each earthquake separately, using estimates of the source wavelet derived by stacking over multiple stations. The results for multiple earthquakes then are stacked to form composite images of the crust and uppermost mantle.

The profiles show clear, continuous signals with times in close agreement with those expected for primary and multiple reflections from the base of coastal plain sediments. Arrivals interpreted as reflections from the Moho increase in travel time from ~10 s beneath the Coastal Plain to 17.4 s (~57 km) beneath the Blue Ridge Mountains, in agreement with trends observed for wide-angle reflections and Ps and Sp arrivals, and provide additional evidence that the Appalachian highlands are in rough isostatic equilibrium. Reflections at 16-20 s (50-75 km) beneath the coastal plain are consistent with layering associated with depletion of the uppermost mantle during Triassic rifting. Reflections at 32-36 s (120-135 km) are roughly 30 km deeper than previous estimates of LAB depth based on Sp receiver functions, but are consistent with the depth to the LAB found in more recent inversions of Ps arrivals and surface waves. Alternatively, these and later reflections at roughly 44 s (~167 km) and 58 s (~224 km) may be due to layering associated with drag-induced flow in the asthenosphere, suggesting largely horizontal rather than vertical flow for depths less than 225 km beneath the Georgia coastal plain.

Acknowledgements

D. N. Verellen was supported by a Chevron research assistantship. We thank our SESAME co-PIs, K. M. Fischer and L. S. Wagner, for helpful discussions, P. Miller, N. Barstow, and G. Slad of the PASSCAL Instrument Center for assistance in the field, our broadband station hosts, and the members of our field crew. This work was supported by the Joseph W. Berg fund and by National Science Foundation grants EAR-0844154 and EAR-1830182.

Data Sources

The waveform data used for this study can be accessed from the IRIS Data Management Center at http://www.iris.edu/SeismiQuery. The network code for the SESAME experiment is "Z9". IRIS Data Services are funded through the Seismological Facilities for the Advancement of Geoscience (SAGE) Award of the National Science Foundation under Cooperative Support Agreement EAR-1851048.

References

Abt, D. L., K. M. Fischer, S. W. French, H. A. Ford, H. Yuan, and B. Romanowicz (2010), North American lithosphere discontinuity structure imaged by Ps and Sp receiver functions, *J. Geophys. Res., 115,* doi:10.1029/2009JB006914.

Barnes A. E., and T. J. Reston (1992), A study of two mid-crustal bright spots from southeast Georgia (USA), *Geophys. J. Int., 108,* 683-691.

Calo, M., T. Bodin, and B. Romanowicz (2016), Layered structure in the upper mantle across North America from joint inversion of long and short period seismic data, *Earth & Planetary Science Letters, 449*, 164-175, doi:10.1016/j.epsl.2016.05.054.

Chowns, T. M. and C. T. Williams (1983), Pre-Cretaceous rocks beneath the Georgia Coastal Plain – Regional implications, in Studies related to the Charleston, South Carolina, earthquake of 1886 – Tectonics and Seismicity, *Geol. Surv. Prof. Paper 1313-L*, 42 pp., U. S. Geol. Survey, Washington, D.C.

Claerbout, J. (1968), Synthesis of a layered medium from its acoustic transmission response, *Geophysics, 33,* 264-269.

Cook, F. A., and K. Vasudevan (2006), Reprocessing and enhanced interpretation of the initial COCORP southern Appalachian traverse, *Tectonophys., 420,* 161-174.

Duff, P. D., and J. N. Kellogg (2017), Reinterpretation of ADCOH and COCORP seismic reflection data with constraints from detailed forward modeling of potential field data – Implications for Laurentia-Peri-Gondwana suture, *Tectonphysics, 712-713,* p. 426-437.

Eaton, D. W., F. Darbyshire, R. L. Evans, H. Grutter, A. G. Jones, and X. Yuan (2009), The elusive lithosphere-asthenosphere boundary (LAB) beneath cratons, *Lithos, 109,* 1-22, doi:10.1016/j.lithos.2008.05.009.

Fischer, K. M., H. A. Ford, D. L. Abt, and C. A. Rychert (2010), The lithosphere-asthenosphere boundary, *Ann. Rev. Earth Planet. Sci., 38,* 551-575, doi:10.1146/annurev-earth-040809-152438.

French, S. W., K. M. Fischer, E. M. Syracuse, and M. E. Wysession (2009), Crustal structure beneath the Florida-to-Edmonton broadband seismometer array, *Geophys. Res. Lett., 36,* L08309, doi:10.1029/2008GL036331.

Gaherty, J. B. and T. H. Jordan (1995), Lehmann discontinuity as the base of an anisotropic layer beneath continents, *Science, 268,* 1468-1471.

Hansen, K. M., K. Roy-Chowdhury, and R. A. Phinney (1988), The sign filter for seismic event detection, *Geophysics, 53,* 1024-1033.

Hatcher, R. D., Jr. (1989), Tectonic synthesis of the U. S. Appalachians, in Hatcher, R. D., Jr., Thomas, W. A., and Viele, G. W., eds., The Appalachian-Ouachita Orogen in the United States, Geological Society of America, The Geology of North America, v. F-2, p. 511-535.

Hatcher, R. D., Jr. (2002), The Alleghanian (Appalachian) orogeny, a product of zipper tectonics: Rotational transpressive continent-continent collision and closing of ancient oceans along irregular margins, in Martinez Catalan, J. R., Hatcher, R. D., Jr., Arenas, R., and Garcia, F. D., eds., Variscan-Appalachian Dynamics: The Building of the Late Paleozoic Basement, Geological Society of America Special Paper 394, p. 199-208.

Hatcher, R. D., Jr. (2010), The Appalachian orogeny: A brief summary, in *From Rodinia to Pangea: the Lithotectonic Record of the Appalachian Region, Geol. Soc. Am. Mem. 206*, edited by R. P. Tollo et al., pp. 1-19. GSA, Boulder, CO.

Hatcher, R. D., Jr., Bream, B. R., and Merschat A. J. (2007), Tectonic map of the southern and central Appalachians: A tale of three orogens and a complete Wilson cycle, in Hatcher, R. D., Jr., Carlson, M. P., McBride, J. H., and Martinez Catalan, J. R., eds., 4-D Framework of Continental Crust, Geological Society of America Memor 200, p. 595-632.

Hawman, R. B. (2008), Crustal thickness variations across the Blue Ridge Mountains, southern Appalachians: An alternative procedure for migrating wide-angle reflection data, *Bull. Seismol. Soc. Am., 98,* 469-475, doi:10.1785/0120070027.

Hawman, R. B., M. O. Khalifa, and M. S. Baker (2012), Isostatic compensation for a portion of the southern Appalachians: Evidence from a reconnaissance study using wide-angle, three-component seismic soundings, *Geol. Soc. Am. Bull., 124,* 291-317, doi:10.1130/B30464.1.

Hedlin, M. A., P. M. Shearer, and P. S. Earle (1997), Seismic evidence for small-scale heterogeneity through the Earth's mantle, *Nature, 387,* 145-150.

Hopper, E., K. M. Fischer, S. Rondenay, R. B. Hawman, and L. S. Wagner (2016), Imaging crustal structure beneath the southern Appalachians with wavefield migration, *Geophys. Res. Lett.,* doi:10.1002/2016GL071005.

IRIS Data Management Center, Incorporated Research Institutions for Seismology, http://www.iris.edu/SeismiQuery.

Iverson, W. P., and S. B. Smithson (1983), Reprocessing and reinterpretation of COCORP southern Appalachian profiles, *E. and Planet. Sci. Lett., 62,* 75-90, doi:10.1016/0012-821X(83)90072-9.

King, P. B. (1961), Systematic pattern of Triassic dikes in the Appalachian region, U. S. Geological Survey Professional Paper 424-B, B93-B95.

Knapp, J. H., D. N. Steer, L. D. Brown, R. Berzin, A. Suleimanov, M. Stiller, E. Luschen, D. L. Brown, R. Bulgakov, S. N. Kashubin, and A. V. Rybalka (1996), Lithosphere-scale seismic image of the southern Urals from explosion-source reflection profiling, *Science, 274,* 226-228.

Langston, C.A. (1979), Structure under Mount Ranier, Washington, inferred from teleseismic body waves, *J. Geophys. Res., 84*, 4749-4762.

Langston, C. A. and J. K. Hammer (2001), The vertical component P-wave receiver function, *Bull. Seismol. Soc. Am., 91,* 1805-1819.

Lehmann, I. (1960), Structure of the upper mantle as derived from the travel times of seismic P and S waves, *Nature, 186,* 956.

Long, M. D., K. G. Jackson, and J. F. McNamara (2016), SKS splitting beneath Transportable Array stations in eastern North America and the signature of past lithospheric deformation, *Geochem. Geophys. Geosyst., 17,* 2-15, doi:10.1002/2015GC006088.

Marzen, R. E., D. J. Shillington, D. Lizarralde, and S. H. Harder (2019), Constraints on Appalachian orogenesis and continental rifting in the southeaster United States from wide-angle seismic data, *J. Geophys. Res., 124,* 6625-6652, doi:10.1029/2019JB017611.

McBride, J. H. (1991), Constraints on the structure and tectonic development of the early Mesozoic South Georgia Rift, southeastern United States: Seismic reflection data processing and interpretation, *Tectonics, 10(5),* 1065-1083, doi: 10.1029/90tc02682.

McBride, J. H., K. D. Nelson, and L. D. Brown (1989), Evidence and implications of an extensive early Mesozoic rift basalt/diabase sequence beneath the southeast Coastal Plain, *Geol. Soc. Am. Bull., 101,* 512-520.

Milkereit, B. (1987), Migration of noisy crustal seismic data, *J. Geophys. Res., 92,* 7916-7930.

Neidell, N. S. and M. T. Taner (1971), Semblance and other coherency measures for multichannel data, *Geophysics, 36,* 482-497.

Parker, E. H., Jr., R. B. Hawman, K. M. Fischer, and L. S. Wagner (2013), Crustal evolution across the southern Appalachians: Initial results from the SESAME broadband array, *Geophys. Res. Lett., 40,* 3853-3857, doi:10.1002/grl.50761.

Parker, E. H., Jr., R. B. Hawman, K. M. Fischer, and L. S. Wagner (2015), Constraining lithologic variability along the Alleghagian detachment in the southern Appalachians using passive-source seismology, *Geology, 43,* 431-434, doi: 10.1130/G36517.1.

Parker, E. H., R. B. Hawman, K. M. Fischer, and L. S. Wagner (2016), Estimating crustal thickness using SsPmp in regions covered by low-velocity sediments: Imaging the Moho beneath the Southeastern Suture of the Appalachian Margin Experiment (SESAME) array, SE Atlantic Coastal Plain, *Geophys. Res. Lett., 43,* doi:10.1002/2016GL070103.

Phinney, R. A. and D. M. Jurdy (1979), Seismic imaging of deep crust, *Geophysics, 44,* 1637-1660.

Pollitz, F. F. and W. D. Mooney (2016), Seismic velocity structure of the crust and shallow mantle of the Central and Eastern United States by seismic surface wave imaging, *Geophys. Res. Lett., 43,* 118-126, doi:10.1002/2015GL066637.

Robinson, E. A. and S. Treitel (1980), Geophysical Signal Analysis, Prentice Hall, New York, 466 pp.

Ruigrok, E. and K. Wapenaar (2012), Global-phase seismic interferometry unveils P-wave reflectivity below the Himalayas and Tibet, *Geophys. Res. Lett., 39,* L11303, doi:10.1029/2012GL051672.

Savage, B., B. M. Covellone, and Y. Shen (2017), Wave speed structure of the eastern North American margin, *Earth Planet. Sci. Lett., 459,* 394-405, doi: 10.1016/j.epsl.2016.11.028.

Schmandt, B., F.-C. Lin, and K. E. Karlstrom (2015), Distinct crustal isostasy trends east and west of the Rocky Mountain Front, *Geophys. Res. Lett., 42,* doi:10.1002/2015GL066593.

Shen, W., and M. H. Ritzwoller (2016), Crustal and uppermost mantle structure beneath the United States, *J. Geophys. Res.*, doi: 10.1002/2016JB012887.

Steer, D. N., J. H. Knapp, L. D. Brown, H. P. Echtler, D. L. Brown, and R. Berzin (1998), Deep structure of the continental lithosphere in an unextended orogen: An explosive-source seismic reflection profile in the Urals (Urals Seismic Experiment and Integrated Studies (URSEIS 1995)), *Tectonics, 17,* 143-157.

Stoffa, P. L., P. Buhl, J. B. Diebold, and F. Wenzel (1981), Direct mapping of seismic data to the domain of intercept time and ray parameter: a plane wave decomposition, *Geophysics, 46,* 255-267.

Till, C. B., L. T. Elkins-Tanton, and K. M. Fischer (2010), A mechanism for low-extent melts at the lithosphere-asthenosphere boundary, *Geochemistry, Geophysics, Geosystems, 11(10)*, doi:10.1029/2010gc003234.

Yang, B. B., Y. Liu, H. Dahm, K. H. Liu, and S. S. Gao (2017), Seismic azimuthal anisotropy beneath the eastern United States and its geodynamic implications, *Geophys. Res. Lett., 44,* 2670-2678, doi:10.1002/2016GL071227.

Yang, Z., A. F. Sheehan, W. L. Yeck, K. C. Miller, E. A. Erslev, L. L. Worthington, and S. H. Harder (2012), Imaging basin structure with teleseismic virtual source reflection profiles, *Geophys. Res. Lett., 39,* L02303, doi:10.1029/2011GL050035.

Yu, Y., J. Song, K. H. Liu, and S. S. Gao (2015), Determining crustal structure beneath seismic stations overlying a low-velocity sedimentary layer using receiver functions, *J. Geophys. Res. Solid Earth, 120,* 3208-3218, doi:10.1002/2014JB011610.

Yuan, H., S. French, P. Cupillard, and B. Romanowicz (2014), Lithospheric expression of geological units in central and eastern North America from full waveform tomography, *Earth and Planet. Sci. Lett., 402,* 176-186, doi:10.1016/j.epsl.2013.11.057.

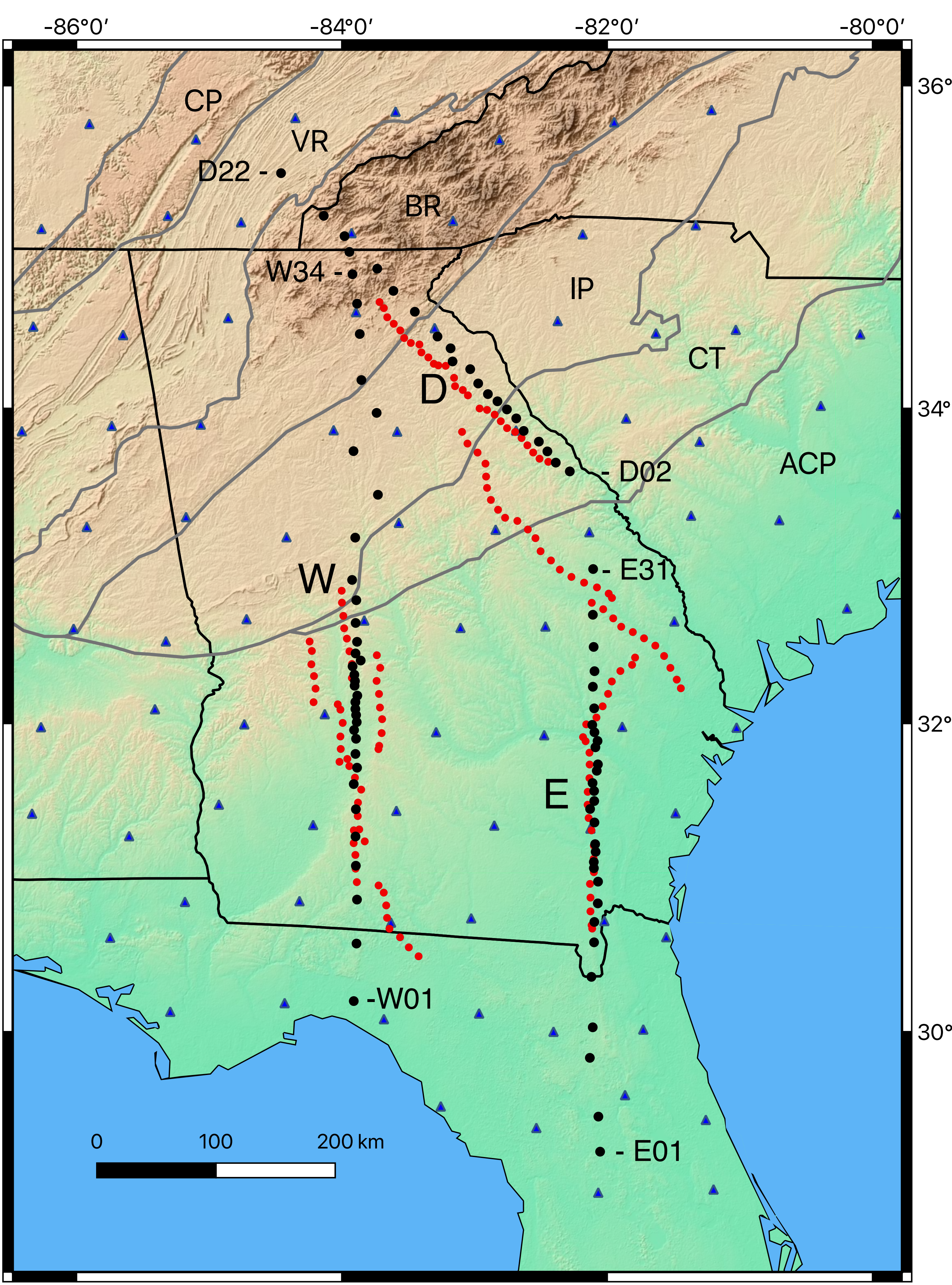
-86°0′
-84°0′
-82°0′
-80°0′
36°0′
34°0′
32°0′
30°0′
CP
VR
BR
D22 -
W34 -
IP
CT
ACP
D
- D02
W
- E31
E
-W01
- E01
0
100
200 km
Figure 1

Figure 1. Map of the study area. Blue dots: SESAME stations along lines W, D, and E. Blue triangles: TA stations. Red dots: subset of stations for overlapping COCORP lines.

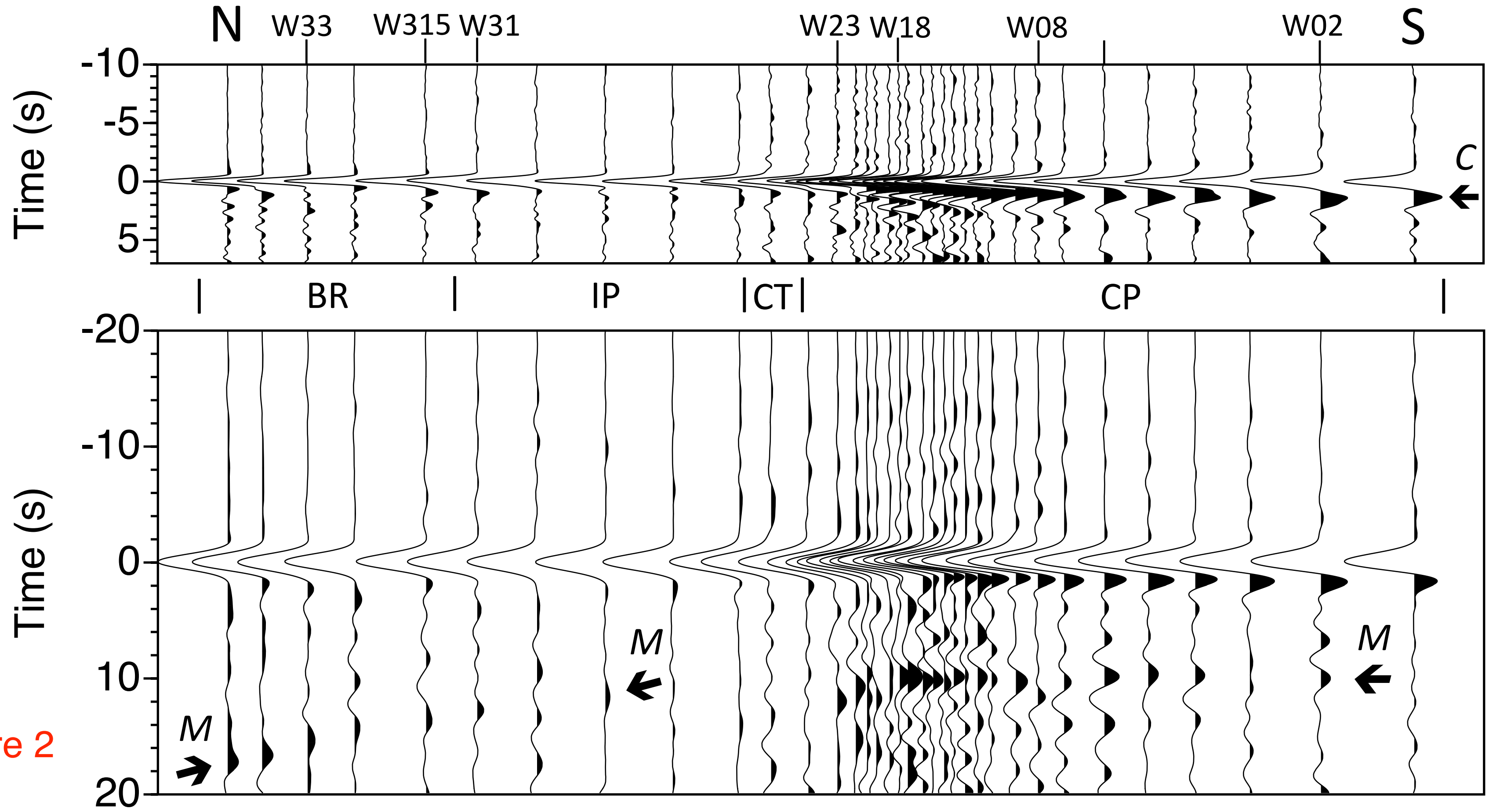
N
W33
W315
W31
W23
W18
W08
W02
S
Time (s)
-10
-5
0
5
C
BR
IP
CT
CP
Time (s)
-20
-10
0
10
20
M
M
M

Figure 2

Figure 2. Stacks of deconvolved records for 16 earthquakes (Table S1) showing PKPdf-generated reflections beneath SESAME Line W, using Gaussian smoothing parameters α=3.0 (top) and 1.0 (bottom). Plotted with reverse polarity (negative polarity for the direct PKPdf arrival at 0 s). Top: "C" is interpreted as the reflection from the base of Cretaceous-Tertiary sediments and poorly consolidated sedimentary rocks. Times are consistent with well data. This reflection merges with the direct arrival near the northern edge of the Coastal Plain. Bottom: "M" is interpreted as the reflection from the Moho, increasing in two-way time from roughly 10 s beneath the Coastal Plain to 17.5 s beneath the Blue Ridge Mountains. A similar trend in crustal thickness is seen at higher frequencies for Line D (Figure S2).

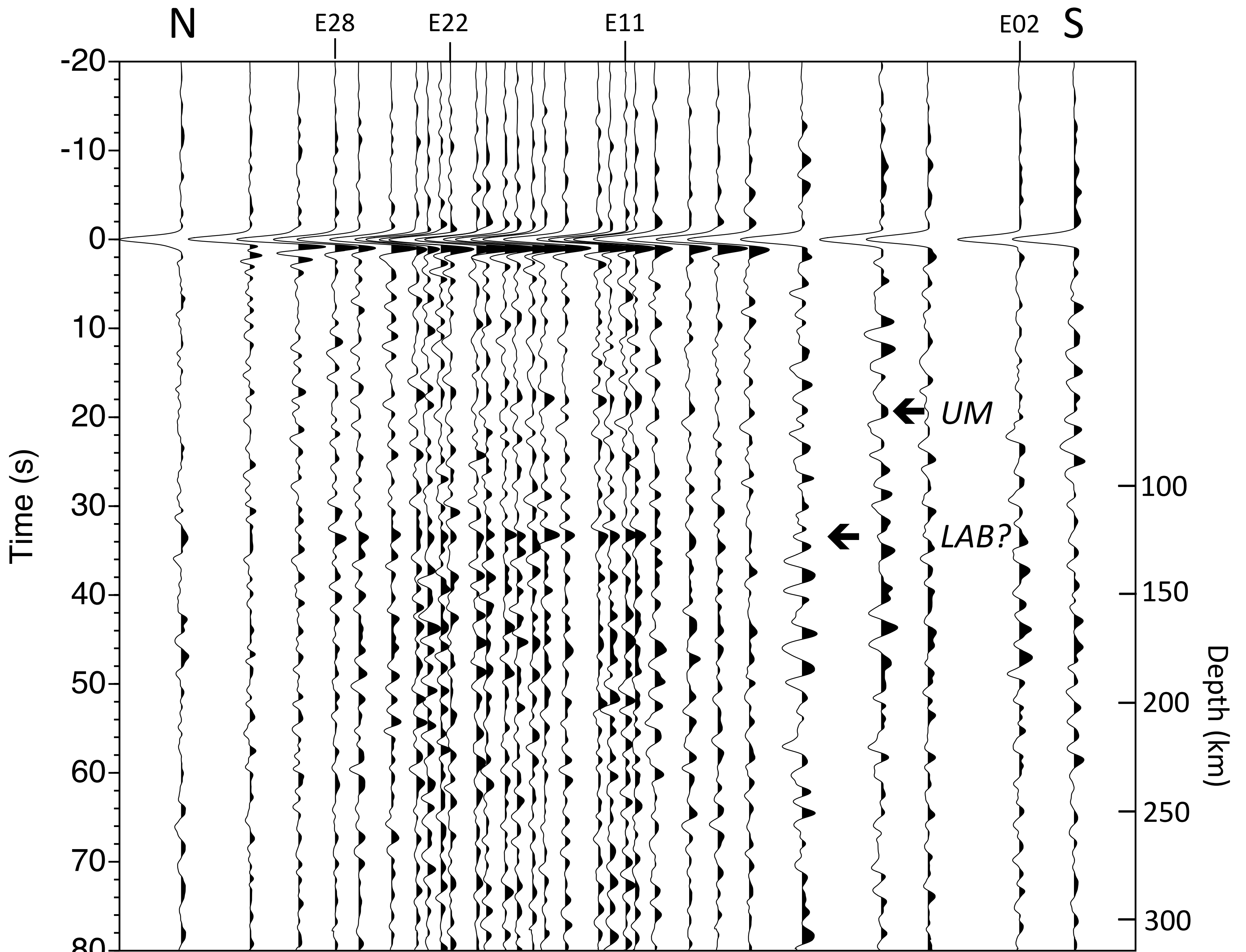
N
E28
E22
E11
E02
S
Time (s)
-20
-10
0
10
20
30
40
50
60
70
80
UM
LAB?
Depth (km)
100
150
200
250
300

Figure 3

Figure 3. Stack of deconvolved records (α=2.0) for 6 earthquakes (Table S1) showing reflections beneath SESAME Line E, plotted with reverse polarity. Depths are approximated using a laterally uniform velocity model (crustal thickness: 55 km; average velocities: 6.5 and 8.1 km/s for the crust and upper mantle, respectively). This approximation contributes 0.5-2.5 km to uncertainties in depth within the mantle. UM: upper mantle reflections. Multicyclic reflections observed at 34–36 s (~127-135 km) may mark the effects of shearing in the vicinity of the LAB and/or intrusions triggered by partial melting of hydrated asthenosphere.

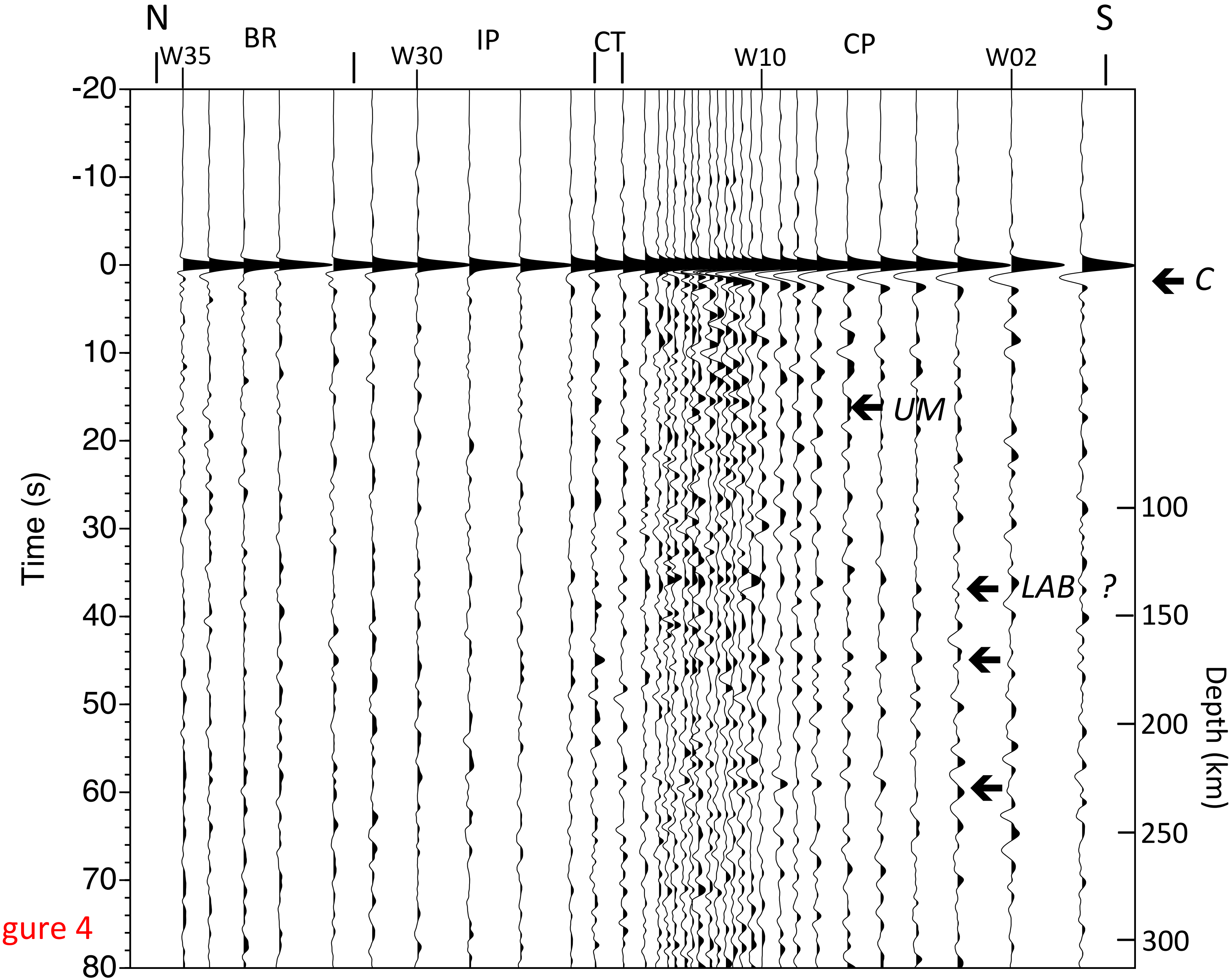

N
S
W35
BR
W30
IP
CT
W10
CP
W02
C
UM
LAB
?
Time (s)
Depth (km)
-20
-10
0
10
20
30
40
50
60
70
80
100
150
200
250
300

Figure 4

Figure 4. Stack of deconvolved records (α=2.0) for 16 earthquakes showing reflections beneath SESAME Line W, plotted with normal polarity (see also Figure S5). C: reflection from the base of Cretaceous and Tertiary sediments and poorly consolidated sedimentary rocks (see also Figure 2). The arrival at 35 s (depth approximately 130 km) is in close agreement with arrivals interpreted as the LAB in Figure 3. Later arrivals at roughly 44 s and 58 s (arrows; ~167 km and 224 km) are interpreted as reflections from layering within the asthenosphere.

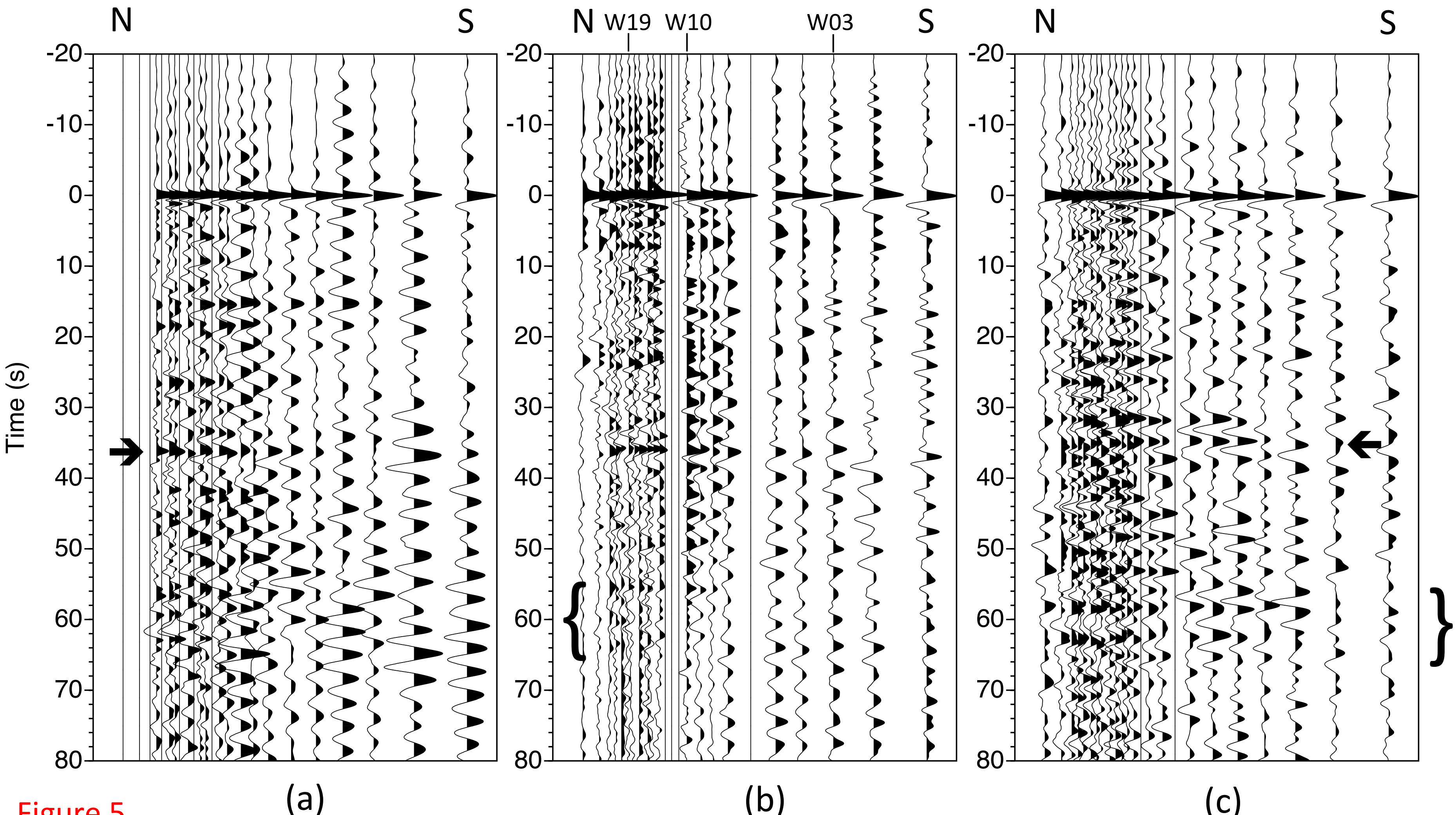

Figure 5

Figure 5. Unstacked, deconvolved sections (α=2.0) for the southern half of SESAME Line W, plotted with normal polarity. Note the agreement in travel time for events at approximately 32-36 s (depth: 120-135 km), interpreted in Figure 4 as reflections from the LAB. See also Figures S6 and S7.

(a) Event 1: Mw=7.3, depth=386 km, Δ = 118°– 120°, back-az = 284°–286°.

(b) Event 5: Mw=6.6, depth=20 km, Δ = 125°– 127°, back-az = 290°– 293°.

(c) Event 9: Mw =6.7, depth=18 km, Δ = 129°– 132°, back-az = 323°- 325°.

Geophysical Research Letters

Supporting Information for

P-wave Reflectivity of the Crust and Upper Mantle Beneath the Southern Appalachians and Atlantic Coastal Plain using Global Phases

Devon N. Verellen[1], Erik C. Alberts[2], Gustavo A. Larramendi, E. Horry Parker, Jr.[3], and Robert B. Hawman

Department of Geology, University of Georgia, Athens, GA, USA

[1]now at Chevron, Houston TX
[2]now at Exxon/Mobil, Houston, TX
[3]now at Black & Veatch, Greenville, SC

Contents of this file

Text S1
Figures S1 to S11
Table S1

Introduction

We show the distribution (Figure S1) and summarize the parameters (Table S1) of earthquakes used in this study and present additional stacked sections for Lines D, E, and W (Figures S2-S5). We then discuss measures of vertical and lateral resolution and investigate the generation of artifacts associated with source-side scattering and differential moveout of PKPdf and PKiKP arrivals (Figures S6-S9). Finally, we describe a simple algorithm for migrating data recorded with unevenly spaced stations and show preliminary results (Figures S10-S11).

Text S1.

1. Additional Stacked Sections

Here we present a map showing the distribution of earthquakes used in this study (Figure S1) and additional stacked sections showing Moho reflections beneath Line D (Figure S2) and Line E (Figure S3) and stacked sections plotted with both normal and reverse polarity to more clearly show reflections from the upper mantle beneath Line E (Figure S4) and Line W (Figure S5).

2. Resolution

Dominant periods in the deconvolved sections range from 1-4 seconds. Quarter-wavelength estimates of vertical resolution range from 1–1.5 km in the crust (Vp = 3.5-6.5 km/s) to 3-8 km in the upper mantle (Vp = 8.1 km/s). Corresponding estimates of lateral resolving power, as measured by the radius of the first Fresnel zone for incident plane waves, range from 3–16 km within the crust to 20-65 km at depths of 70-250 km within the mantle. Lateral resolving power will also depend on station spacings, which vary from 3.5-42 km along the W line, 4.5–43 km along the E line, and 5–29 km along the D line. For future work, projections of TA stations (Figure 1) onto the SESAME lines will be used to fill in some of the gaps in coverage [*Hopper et al.,* 2016].

3. Processing Artifacts: Comparison of Deconvolution, Autocorrelation, and Crosscorrelation for Long-Duration Effective Source Wavelets

Effective source wavelets for the shallower-focus earthquakes used in this study include significant energy associated with underside reflections, e.g., pPKPdf and sPKPdf, in the source region. Here we examine the ability of deconvolution to recover reflections at later two-way times where portions of the effective source wavelets extend beyond the listening window. To examine this issue, we use the estimates of source wavelets derived by stacking waveforms for stations deployed north of the Coastal Plain, as described in the main text, for all the earthquakes listed in Table S1. We construct synthetic seismograms by convolving these estimates with a series of 6 impulses representing the direct PKPdf arrival and a pseudo-random time distribution of 5 reflections, then add low-level (S/N ~ 10) random noise. Reflections are assigned a uniform amplitude, equal to half that of the direct arrival. We then deconvolve each seismogram using the input source wavelet and a range of Gaussian smoothing parameters ($\alpha = 1.0 - 4.0$).

The results for most of the earthquakes show clear pulses at the expected travel times for the four earliest reflections, along with various levels of noise between reflections and before the direct arrival. As expected, for later reflections where the effective source wavelets extend beyond the listening window, reflection amplitudes are not fully recovered (Figures S6c – S6g). This can also generate spurious energy in the later portions of the traces (e.g., Figure S6c). Stacking the traces, using the same combinations of earthquakes used to generate the stacks of real data in Figures 2-4 and S2-S5, suppresses these artifacts (Figure S7).

Autocorrelation of the same input traces also recovers reflections but with higher levels of noise; in this case, the noise is more evenly distributed over the length of each trace. As expected, cross correlation of the input trace with the effective source wavelet is more successful than autocorrelation in recovering reflection amplitudes, but sidelobes remain a problem because of narrower bandwidths compared with the deconvolved traces. This is particularly evident for events 9 and 7 (Figures S6e and S6f). Again, stacking helps to suppress this noise (Figure S7).

As noted in the text, the estimation of effective source wavelets can be complicated by the arrival of two phases (PKPdf and PKiKP) in the time window of interest. For a source depth of 100 km and distances of 115°-140°, travel times for the two phases differ by ~ 0-3 s and ray parameters differ by 0.01–0.26 s/°. For the earthquakes used in this study, the effective array apertures for stations deployed north of the Coastal Plain ranged from 1.7°–2.6° and the differential moveouts ranged from 0.1-0.4 s. The stacking procedure described in the text treats all these phases (including source-side scattering) as a single arrival and therefore yields an effective source wavelet of extended duration, with some loss of resolution at higher frequencies. Differential moveouts for PKPdf and PKiKP between those stations and the southernmost stations range from 0.1-1.1 s; this causes some broadening of deconvolved waveforms (Figure S8) that is minimized by stacking (Figure S9).

4. Migration

4.1. Migration Method

As noted in the main text, stacking of waveforms for multiple earthquakes may degrade rather than enhance some signals. To preserve signal levels and to construct a more complete image of reflectivity, we migrate events observed for individual earthquakes and then stack the results to form composite cross sections. However, as noted in the above discussion of processing artifacts, care must be exercised before incorporating coherent energy observed in the later portions of the sections.

After deconvolving waveforms for a given earthquake, we divide the traces along each line (D, E, and W) into shorter-aperture gathers (to allow for local variations in travel times and apparent dips of reflections) and slant stack to obtain objective measures of apparent slowness and coherence of reflected arrivals. Reflections are assumed to arrive as plane waves across each subset of stations. Coherence is measured using semblance [*Neidell and Taner,* 1971]. Following *Stoffa et al.* [1981], we then apply a coherency filter derived from the smoothed semblance to suppress noise. Alternative measures of coherence such as signal polarity [*Hansen et al.,* 1988] can also be used. The choice of coherency thresholds is based on the levels required to fully suppress noise preceding the direct arrival.

Standard migration algorithms require input traces that are evenly spaced. Because this requirement is violated by the SESAME array, we are experimenting with alternative methods. For the examples shown in Figures S10 and S11, we use a modification of an approach developed for sparse wide-angle reflection data [*Hawman,* 2008]. This somewhat rudimentary algorithm is based on a simple line drawing but retains some characteristics of the original wavefield. In common with methods developed by *Phinney and Jurdy* [1979] and *Milkereit* [1987], it uses the slant stack as an intermediate data set. As implemented here, apparent horizontal slownesses are measured relative to the zero slowness value assigned to the aligned first arrival (PKPdf). The algorithm treats each sample in the coherency-filtered slant stack as a reflection from an interface at depth. Each reflection is assumed to arrive as a plane wave across the input subsection. The algorithm proceeds by downward continuing each sample through an assumed velocity model along a ray defined by the appropriate positive or negative horizontal slowness. A reflector segment then is constructed with a dip determined by the horizontal slowness and layer velocity and a width controlled by the subsection aperture and Fresnel radius. The process then is repeated for neighboring (or overlapping) subsections to build a subsurface image. The edges of individual reflector segments sometimes show concave upward curvature. These “smiles” are measures of the degree of smearing of individual peaks in the slant stack and thus serve as useful measures of the resolving power of the component subsections [*Hawman,* 2008] and scatter in travel times due to statics variations.

Migration velocity models are constructed for different stations along the SESAME array using a combination of COCORP images of Triassic rift basin and Coastal Plain sediments [*McBride et al.,* 1989; *Barnes and Reston,* 1992] and previous wide-angle [*Hawman et al.,* 2012] and SsPmp [*Parker et al.,* 2016] analyses of the study area for the crystalline crust. For the preliminary images shown here, we used a constant value of 8.1 km/s for the velocity of the upper mantle. As expected for the nearly vertical incidence angles for PKPdf/PKiKP, most of the coherent energy in the slant stacks is concentrated at very small apparent slownesses (-0.05 to +0.05 s/km), corresponding to small apparent dips. The partial migrated images from individual trace subsections then are summed to construct a composite migrated section (Figures S10 and S11).

Gaps in subsurface coverage due to inactive stations are gradually filled in by stacking results for multiple earthquakes. For stations deployed in the Coastal Plain, we are also experimenting with predictive deconvolution [*Robinson and Treitel,* 1980; *Yu et al.,* 2015] to suppress multiples generated within Cretaceous and younger sediments and underlying Triassic/Jurassic extensional basins.

4.2. Preliminary Migration Results

Preliminary migrated images (Figures S10 and S11) are based on vertical stacks for 7-8 earthquakes, with no contributions from TA stations, and therefore are rather sparse. They will certainly change as more events are added. Although the migration velocity models incorporate layers representing low-velocity sediments of the Coastal Plain and underlying rift basins, no attempt has been made to remove the effects of multiples generated within those sequences. At the risk of reading too much into the results at this early stage of analysis, we note the following:

1) The section for Line W across the Atlantic coastal plain shows concentrations of reflections at depths of 50-75 km (just below Moho), 90-110 km, 140-160 km, 180-200 km, and 250-270 km (Figure S10).

2) The section for Line D, trending NW across the Carolina Terrane, Inner Piedmont, and Blue Ridge shows a similar clustering of reflections at depths greater than 90 km, but the zone of highly reflectivity at 50-75 km is absent (Figure S11). One possible interpretation is that the 50-75 km zone beneath the Coastal Plain represents layers within the upper mantle depleted by partial melting during Mesozoic extension and underplating of the crust [*Pollitz and Mooney,* 2016]. The absence of this zone beneath Line D (Figure S11) would be consistent with more limited extension of inboard terranes, as suggested by the lack of Triassic dikes northwest of the Inner Piedmont [*King,* 1961]. More detailed tracking of this zone, in particular, using wide-angle reflections to constrain lower crustal velocities (e.g., *Marzen et al*., 2019) could be used to help establish the northwest extent of major alteration of the crust and uppermost mantle associated with the breakup of Pangaea.

3) Overall, the sections over the Carolina Terrane, Inner Piedmont, and Blue Ridge (Line D and northern half of Line W) show a concentration of reflectors at depths of roughly 140-160 km, consistent with shearing just below the LAB and in agreement with recent tomography results that show a roughly 150-km thick lithosphere beneath the Grenville province and Appalachian Mountains [*Savage et al.,* 2017].

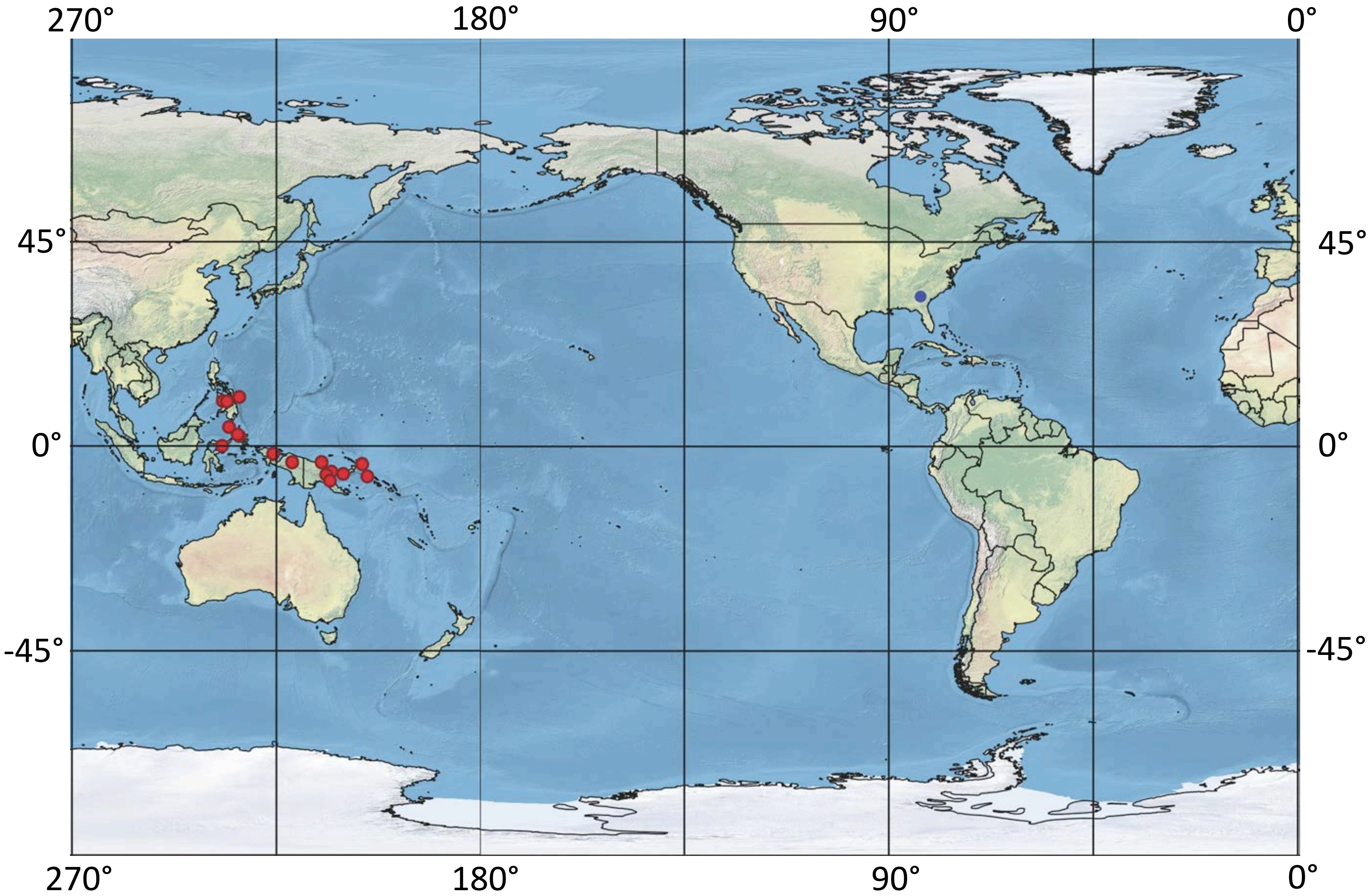

Figure S1

Figure S1. Locations of 16 earthquakes (red circles) used for the analysis of PKPdf - generated reflections. Blue circle indicates the average location of SESAME stations.

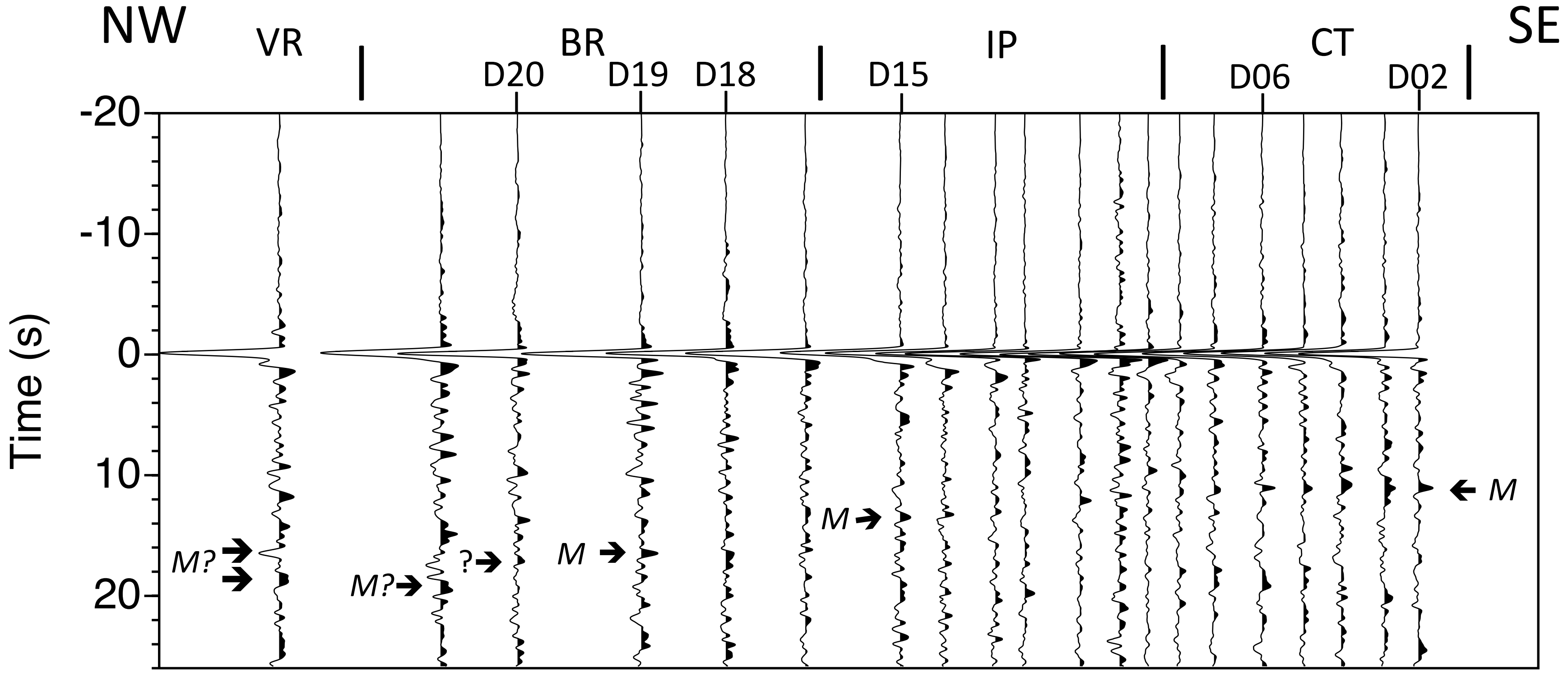

Figure S2

Figure S2. Stacks of deconvolved records (α=4.0) for 16 earthquakes (Table S1) showing PKPdf-generated reflections beneath SESAME Line D. Stations D01 and D16 were never deployed. Prior to stacking, traces were normalized by the RMS value for the 18-s noise window preceding the direct PKPdf arrival to give greater weight to seismograms with higher signal levels. Samples have been multiplied by a factor equal to the square root of two-way time to smoothly increase amplitudes for later reflections. The arrival at 0 s is the deconvolved waveform for PKPdf. Upon reflection at the free surface, this arrival reverses polarity. Therefore, reflections from positive impedance contrasts (lower velocity over higher velocity) will have a polarity opposite to the polarity of PKPdf.

The stack is plotted with reverse polarity (negative polarity for the direct PKPdf arrival). M: pulse interpreted as the reflection from the Moho. This increases in travel time from 11.2 s (crustal thickness: 36.4 km, assuming an average P-wave velocity of 6.5 km/s) at station D02 (Carolina Terrane) northward to 13.5 s (43.9 km) at station D15 (Inner Piedmont). These times are consistent (to within 0.1 – 0.3 s) with arrivals interpreted as Moho reflections in coincident, reprocessed COCORP lines [*Cook and Vesudevan,* 2006]. Those authors were not able to identify Moho north of station D18, but the stacked section shows strong arrivals interpreted as Moho reflections at station D19 (16.5 s) and D20 (17.2 s) in the Blue Ridge Mountains. Corresponding crustal thicknesses, again assuming an average P-wave velocity of 6.5 km/s, are 54 and 56 km. This increase mimics the trend observed for Line W (Figure 2). These estimates are also consistent with values obtained from Ps receiver functions that suggest a similar increase in crustal thickness from 36.2 km at station D02 to 57 km at station D20 [*Parker et al.,* 2013; 2015]. They are also consistent with earlier estimates derived from wide-angle data [*Hawman et al.,* 2012], suggesting that the southern Appalachian highlands are in rough isostatic equilibrium.

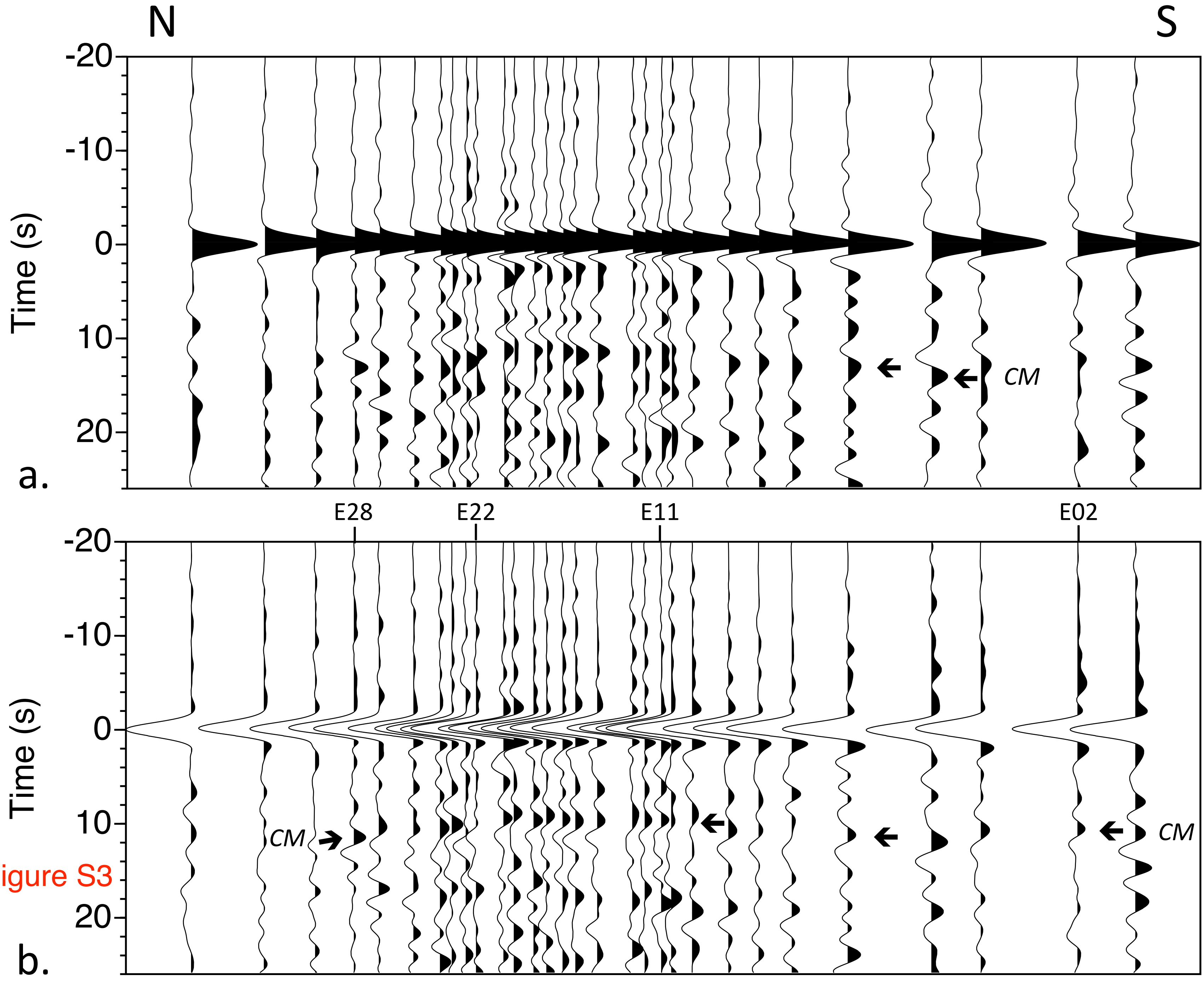
N
S
-20
-10
0
10
20
Time (s)
CM
a.
E28
E22
E11
E02
-20
-10
0
10
20
Time (s)
CM
CM
b.
Figure S3

Figure S3. Stacks of deconvolved records (α=1.0) for 8 earthquakes (Table S1) for SESAME Line E (deployed a year after Lines W and D). Station E14 was never deployed. The stack is plotted with both normal and reverse polarity to more clearly show the reflections.

a) Stack plotted with normal polarity (positive polarity for the direct PKPdf arrival).
b) Stack plotted with reverse polarity (negative polarity for PKPdf).
Assuming a simple first-order discontinuity, the Moho would be expected to generate a positive polarity reflection on the reverse polarity sections. Travel times for this pulse are 10.4 – 10.6 s for stations E02 and E03, then decrease to a minimum of 8.9 – 9.9 s for stations E11 – E22. Moho times along coincident COCORP stations [*McBride,* 1991] are greater, between (10.5 – 11.3 s); as suggested for Line W, the disparity may be due in part to the broader depth range of reflectors sampled by the broader PKPdf-generated waveforms. From E23 to E28, Moho times increase from 10.1 – 11.4 s, in better agreement with the COCORP times (10.5 – 11.6 s). The Moho times observed in this study agree to within 0.1 – 1.7 s with normal-incidence times predicted for models derived from SsPmp arrivals [*Parker et al.,* 2016]. Taken together, the multicyclic reflections “CM" at roughly 9-12 s on the normal and reverse polarity sections are interpreted as a layered crust-mantle transition at depths of approximately 30-37 km.

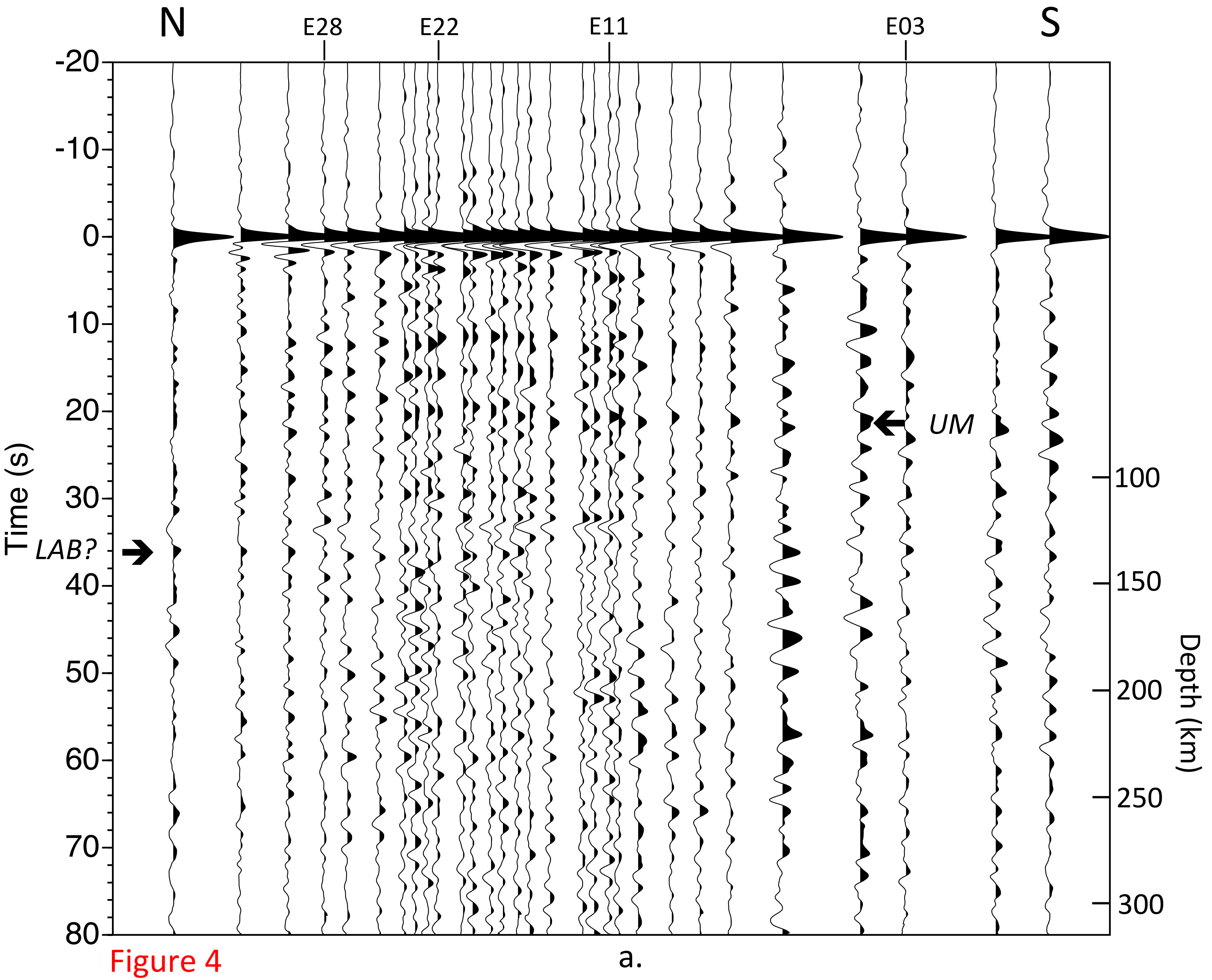
N
E28
E22
E11
E03
S
-20
-10
0
10
20
30
40
50
60
70
80
Time (s)
LAB?
UM
100
150
200
250
300
Depth (km)
a.
Figure 4

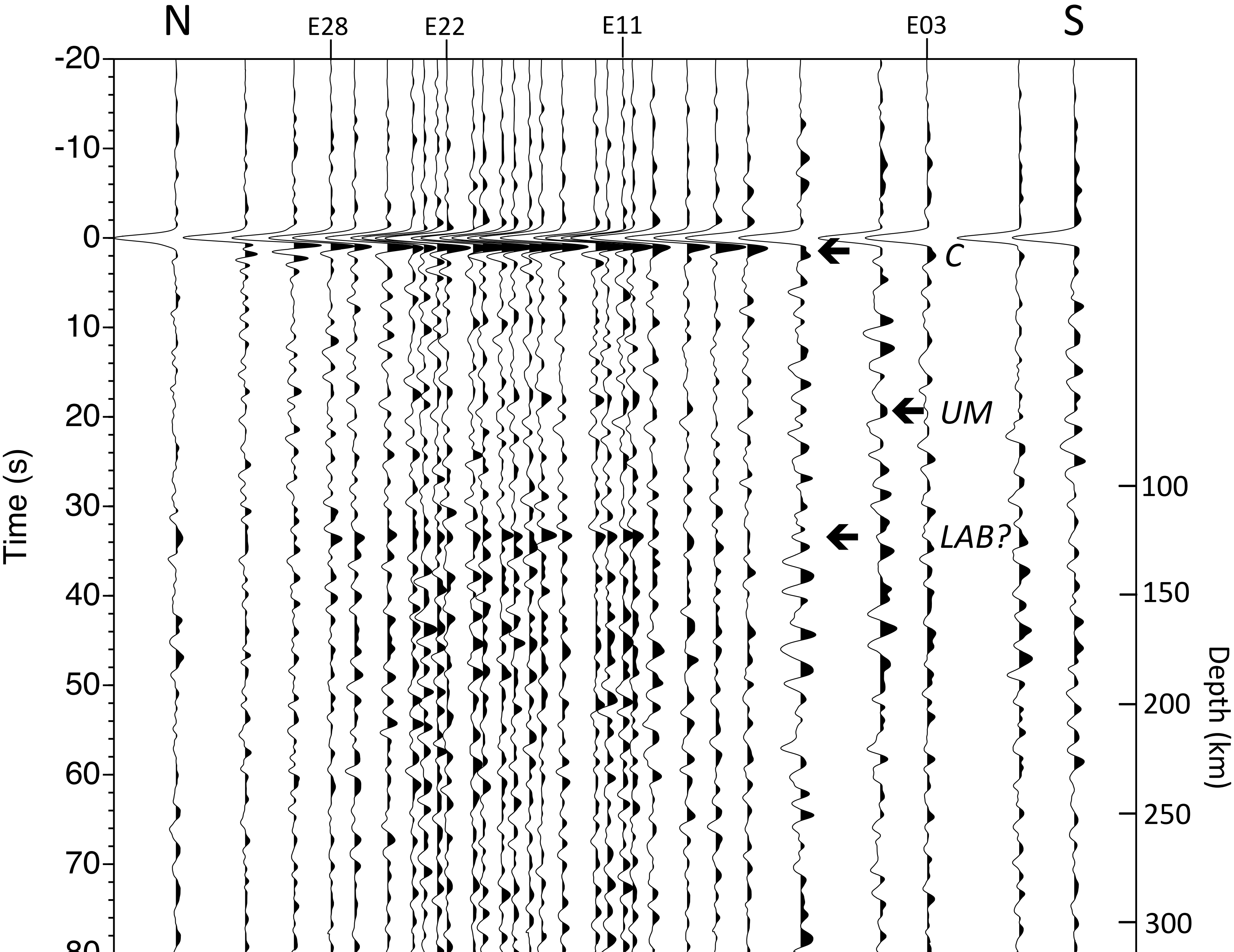
N
E28
E22
E11
E03
S
Time (s)
-20
-10
0
10
20
30
40
50
60
70
80
C
UM
LAB?
Depth (km)
100
150
200
250
300
Figure S4
b.

Figure S4. Stacks of deconvolved records (α=2.0) for 6 earthquakes (Table S1) showing PKPdf-generated reflections from the crust and uppermost mantle beneath SESAME Line E. Station E14 was never deployed. Plotted with both normal and reverse polarity to more clearly show the reflections. Depths are approximated using a laterally uniform velocity model with a crustal thickness of 55 km and average velocities of 6.5 km/s for the crust and 8.1 km/s for the upper mantle. This approximation contributes 0.5-2.5 km to uncertainties in depth within the mantle. (a) Plotted with normal polarity. (b) Plotted with reverse polarity (same as Figure 3). C: interpreted as the reflection from the base of Cretaceous-Tertiary sediments and poorly consolidated sedimentary rocks. Times are consistent with well data. Reflections from the crust-mantle transition are more clearly shown in Figure S3. UM: reflections arriving between 16 and 20 s, possibly generated by layers within the uppermost mantle depleted by partial melting during Mesozoic extension [*Pollitz and Mooney,* 2016]. Multicyclic reflections observed at 34–36 s (~127-135 km) may mark the effects of shearing in the vicinity of the LAB and/or intrusions triggered by partial melting of hydrated asthenosphere.

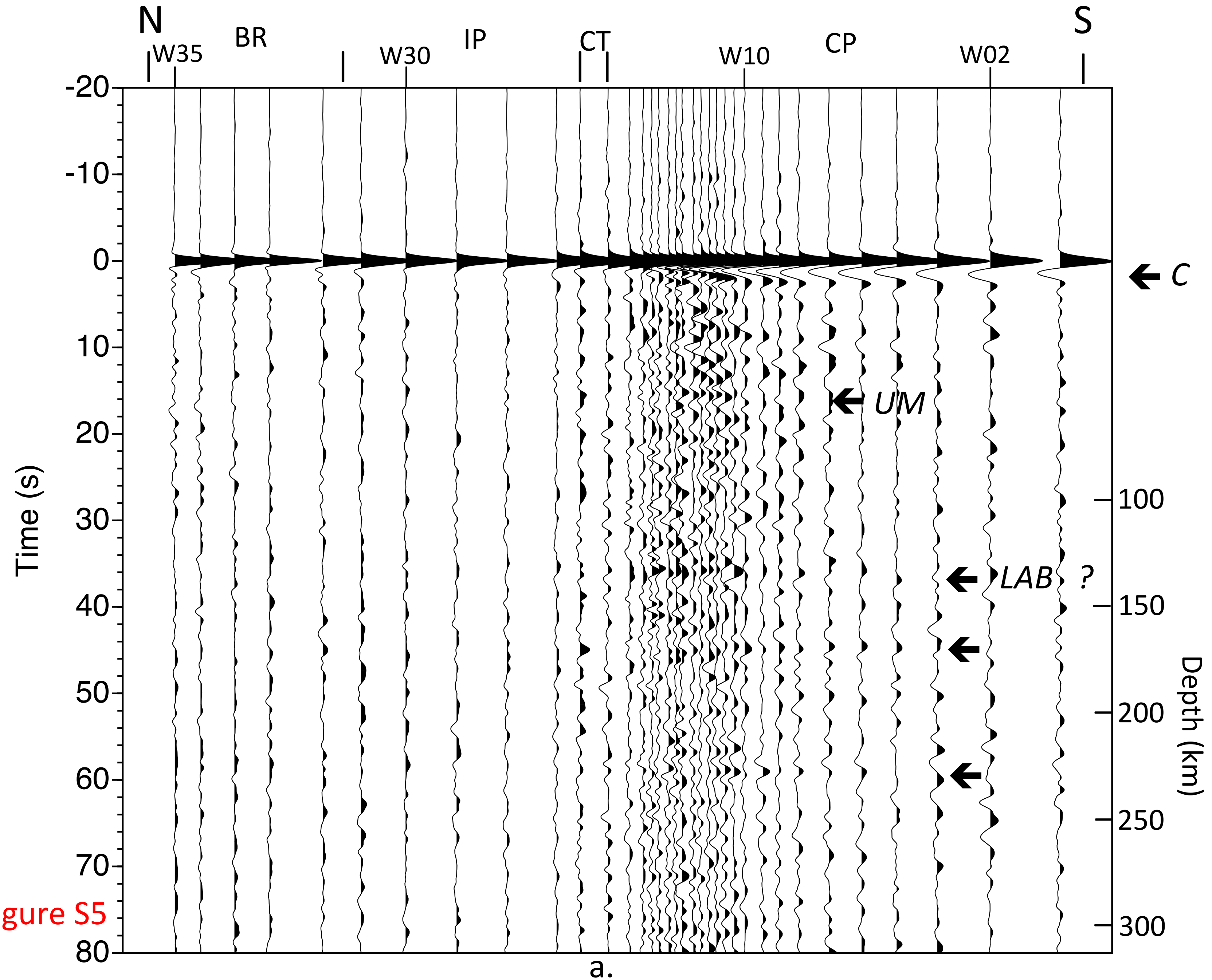
N
S
W35
BR
W30
IP
CT
W10
CP
W02
Time (s)
-20
-10
0
10
20
30
40
50
60
70
80
Depth (km)
100
150
200
250
300
C
UM
LAB
?
a.
Figure S5

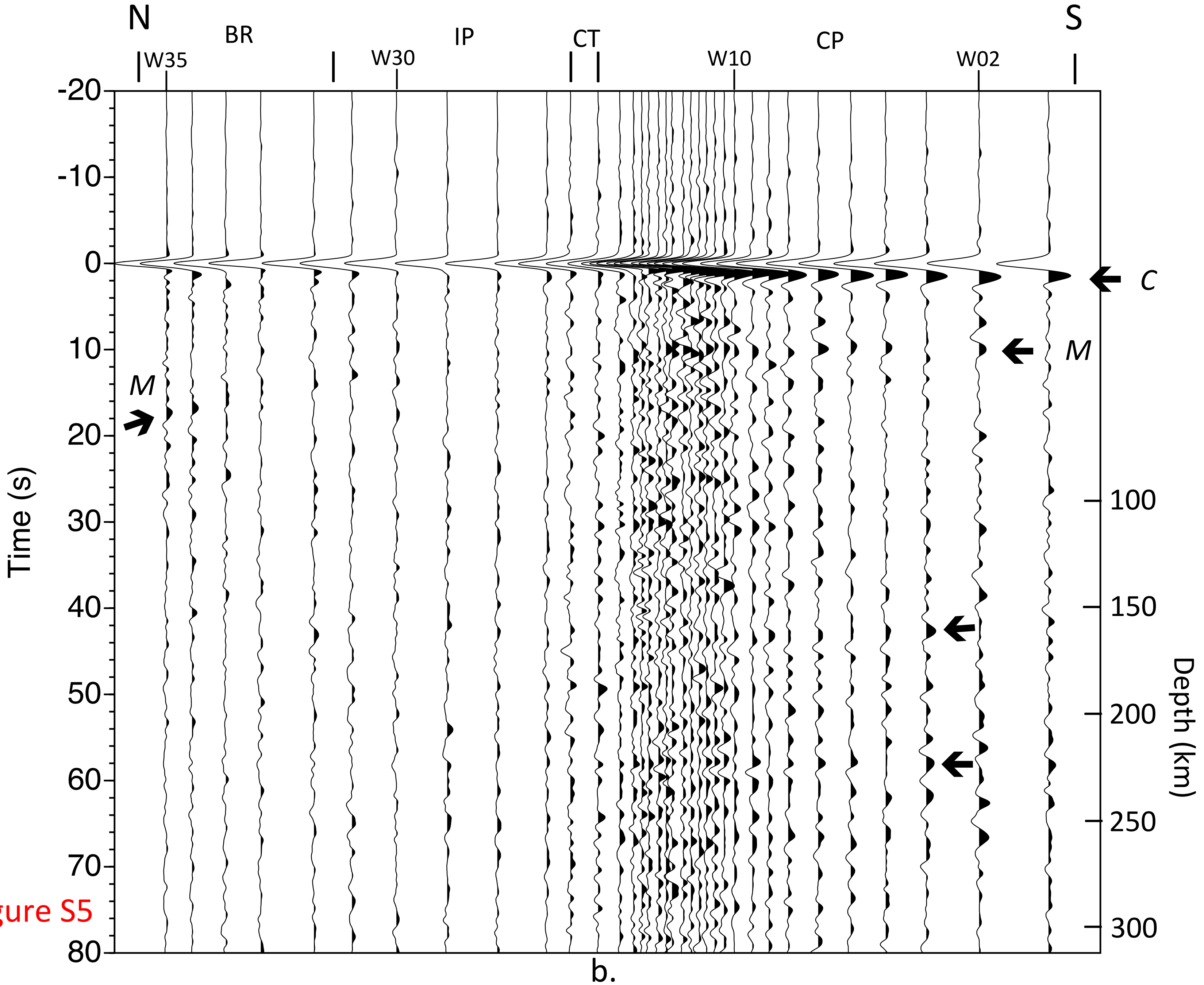

N
S
BR
IP
CT
CP
W35
W30
W10
W02
Time (s)
Depth (km)
C
M
M
-20
-10
0
10
20
30
40
50
60
70
80
100
150
200
250
300
b.

Figure S5

Figure S5. Stacks of deconvolved records (α=2.0) for 16 earthquakes (Table S1) showing PKPdf-generated reflections from the crust and upper mantle beneath SESAME Line W, plotted with both normal and reverse polarity to more clearly show the waveforms. Station W25 was never deployed. (a) plotted with normal polarity (same as Figure 4). UM: reflection from the uppermost mantle, less continuous than the event observed beneath Line E (Figure S4). C: reflection from the base of Cretaceous and Tertiary sediments and poorly consolidated sedimentary rocks (see also Figure 2). This arrival shallows towards the north and projects to the surface near the observed feather edge of Coastal Plain sediments. (b) plotted with reverse polarity. M: arrival interpreted as the reflection from the Moho (see also Figure 2). The arrival at 35 s (depth approximately 130 km) is in close agreement with arrivals interpreted as the LAB in Figure S4b. Later arrivals (arrows) at roughly 44 s and 58 s (~167 km and 224 km) are interpreted as reflections from layering within the asthenosphere.

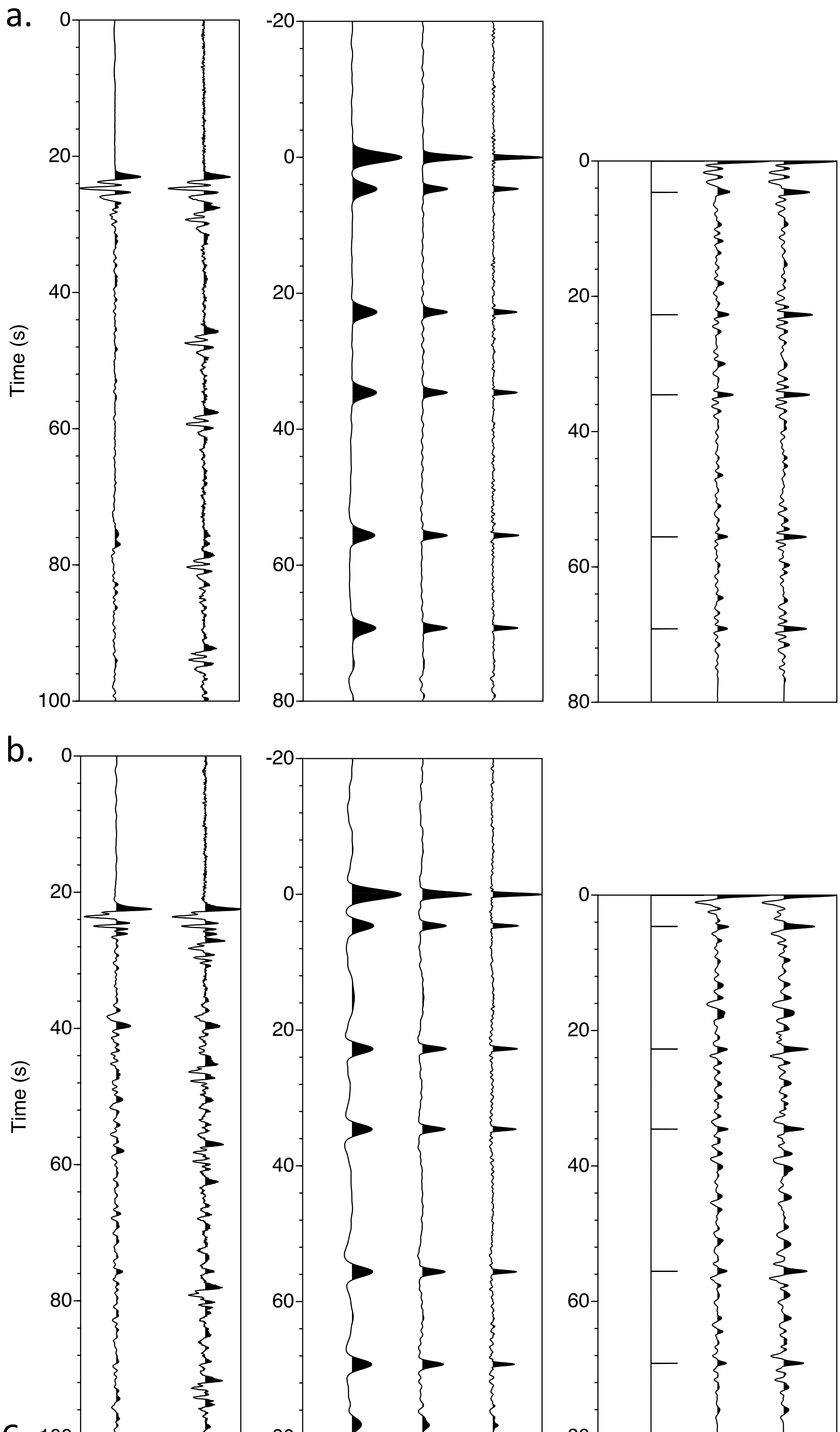

Figure S6

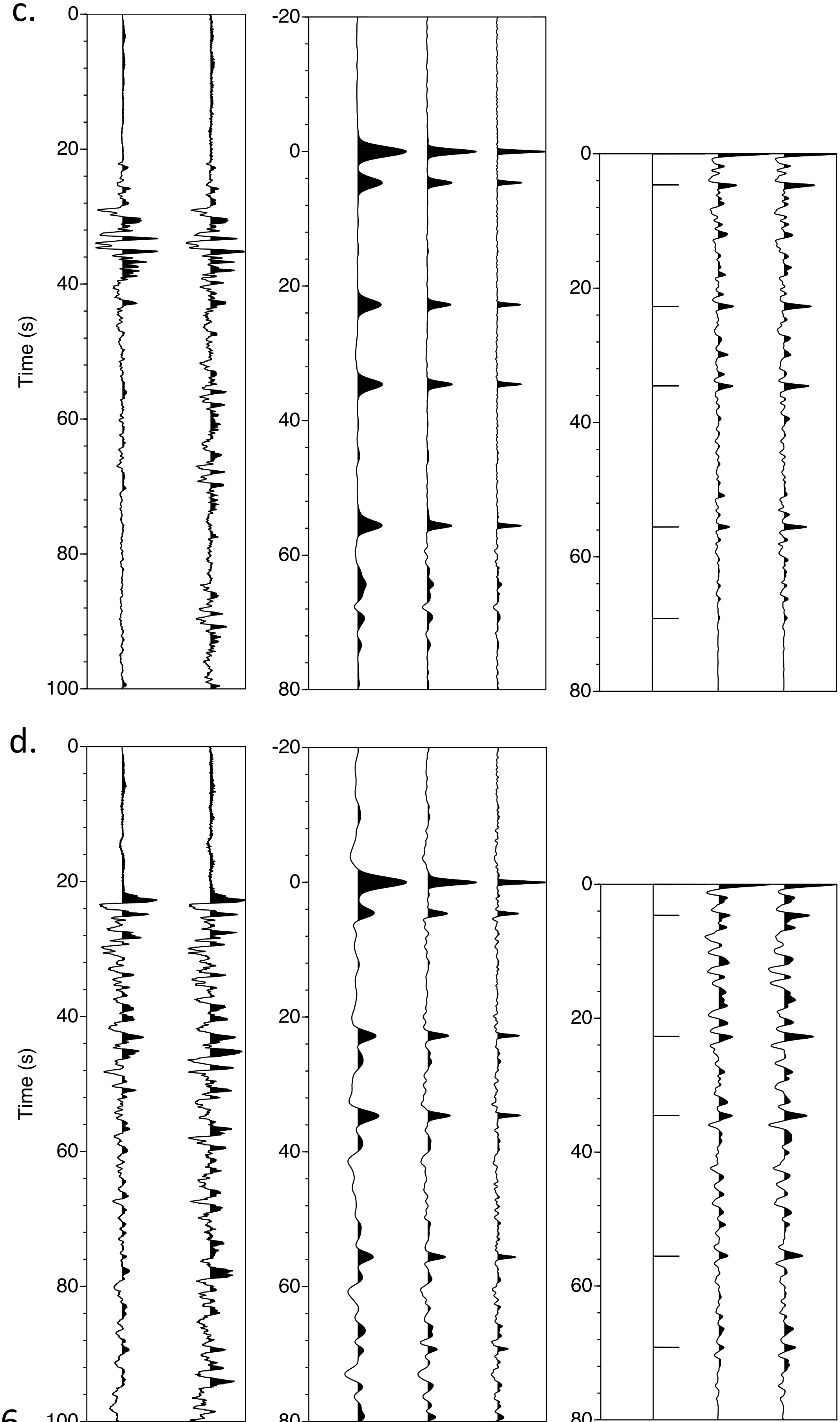

Figure S6

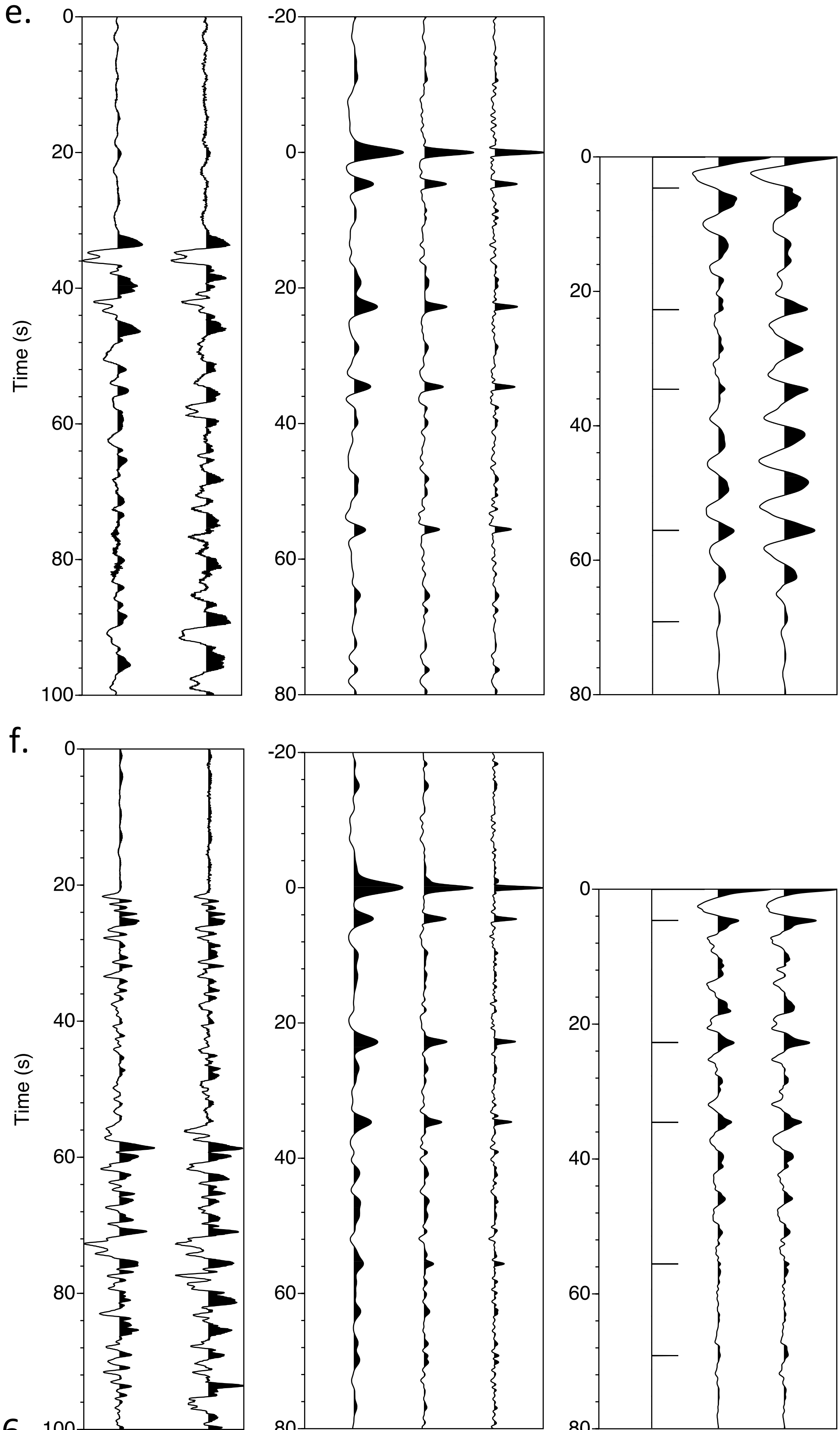

Figure S6

g.

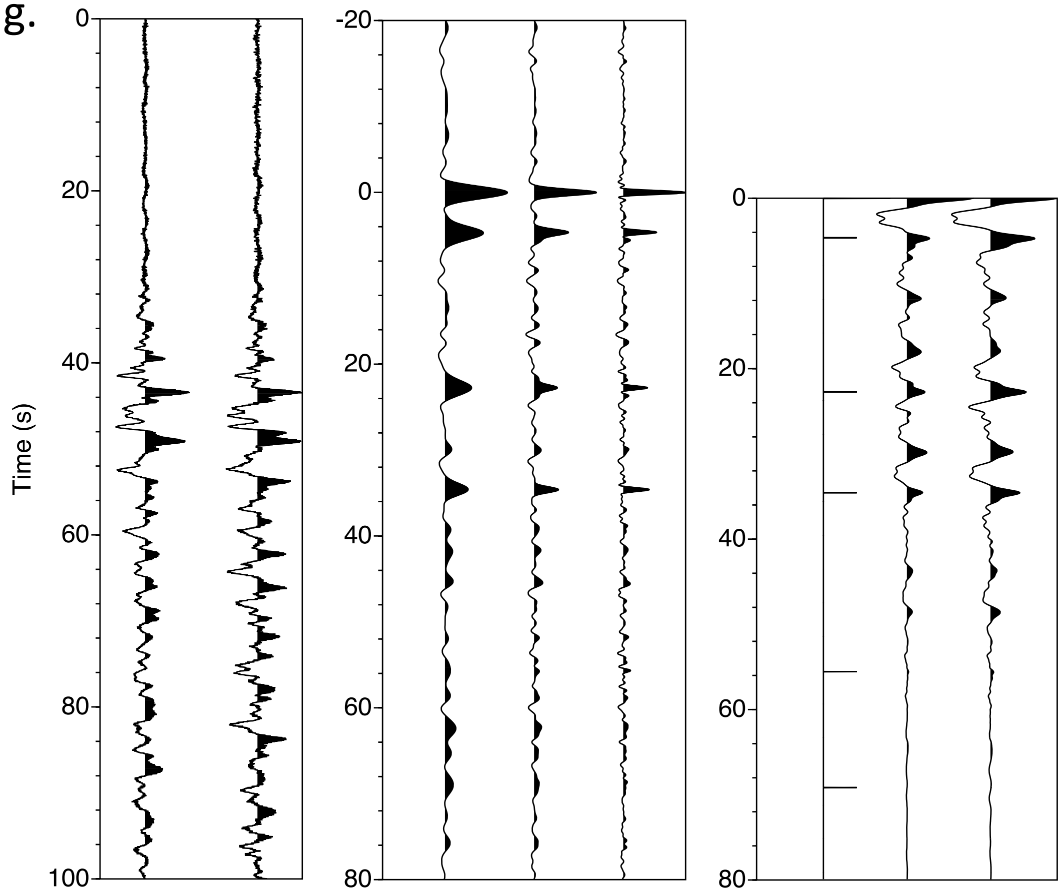

Figure S6

Figure S6. Comparison of deconvolution, autocorrelation, and cross correlation for long-duration effective source wavelets. Results are shown for seven representative earthquakes (events 4, 3, 1, 2, 9, 7, and 5) (Table S1). Effective source wavelets (left panel, first trace) were derived by stacking waveforms for broadband stations deployed north of the Atlantic Coastal Plain (Figure 1). Synthetic seismograms (second trace) then were generated by convolving the effective source wavelets with a series of 6 impulses representing the direct PKIKP (PKPdf) arrival and a pseudo-random time distribution of five reflections, then adding low-level (S/N ~ 10) random noise. The middle panel shows the synthetic seismograms deconvolved in the frequency domain by the effective source wavelet using a water-level of 0.001 and a range of Gaussian smoothing parameters (α = 1, 2, 4). The beginning and end of traces were linearly tapered over a window of 3 s prior to Fourier transformation. The righthand panel shows the 6 impulses (first trace) used to generate the synthetic seismograms, the zero and positive lags of the autocorrelation (second trace) of the synthetic seismogram, and the zero and positive lags of the cross correlation (third trace) of the synthetic seismogram with the effective source wavelet.

a. Results for event 4 (Mw = 6.9; source depth: 208 km; predicted differential time between pPKPdf and PKPdf: ~54 s). Deconvolution recovers the amplitudes of all 5 reflections, with minimal spurious energy over other portions of the seismograms. Autocorrelation also recovers the 5 reflections but not with their full amplitude, and also generates appreciable sidelobes. Cross correlation is better than autocorrelation in recovering amplitudes but sidelobes remain.

b. Results for event 3 (Mw=6.6; source depth: 62 km: predicted differential time between pPKPdf and PKPdf: ~18 s). Deconvolution again recovers the amplitudes of all 5 reflections, but an artifact is generated at the end the trace, where the source-side reflection pPKPdf for the latest event extends past the listening window. Reflections are barely above the level of sidelobes in the autocorrelation, but reflection amplitudes are better recovered by cross correlation. The decrease in the number of samples contributing to the correlations at greater lags suppresses the noise pulse at the end of the trace.

c. Results for event 1 (Mw=7.3; source depth: 386 km; predicted differential time between pPKPdf and PKPdf: ~134 s). Although source-side scattering for this event begins well after the end of the listening window, the large magnitude generates an effective source wavelet with a duration greater than 20 s, with much of the energy delayed until the middle of the waveform. As a result, the latest reflection at roughly 70 s is just barely recovered and is accompanied in the deconvolved output by artifacts. As with event 3 (Figure S6b), these artifacts do not appear in the correlated traces.

d. Results for event 2 (Mw=7.1; source depth: 61 km; predicted differential time between pPKPdf and PKPdf: ~17 s). The results are similar to those for event 1 (Figure S6c), but in general are noisier.

e. Results for event 9 (Mw=6.7; source depth: 18 km; predicted differential time between pPKPdf and PKPdf: ~6 s). For this event and event 5 (Figure S6g), the input trace started roughly 30 s before the onset of PKPdf, rather than 20 s as used for other events, resulting in a shorter listening window (70 s rather than 80 s). The latest reflection is no longer recovered. For the deconvolved traces, the noise level is similar to that for event 2 (Figure S6d). Correlated traces have a much narrower bandwidth that is dominated by lower frequencies in the effective source wavelet. As a result, the earliest reflection is not recovered in those traces.

f. Results for event 7 (Mw=7.1; source depth: 129 km: predicted differential time between pPKPdf and PKPdf: 34 s). Results are similar to those for event 9 (Figure S6e), but because most of the energy is concentrated over later portions of the effective source wavelet, the amplitude of the fourth reflection is not as well recovered in the deconvolved traces. Compared with event 9, the greater bandwidth of the source wavelet results in broader band reflections in the correlated traces.

g. Results for event 5 (Mw=6.6; source depth: 20km; predicted differential time between pPKPdf and PKPdf: 7 s). As with event 9 (Figure S6e), the input trace for this event started roughly 30 s before the onset of PKPdf. Coupled with the emergent nature of the source waveform, this results in barely detectable signal levels for the two latest reflections.

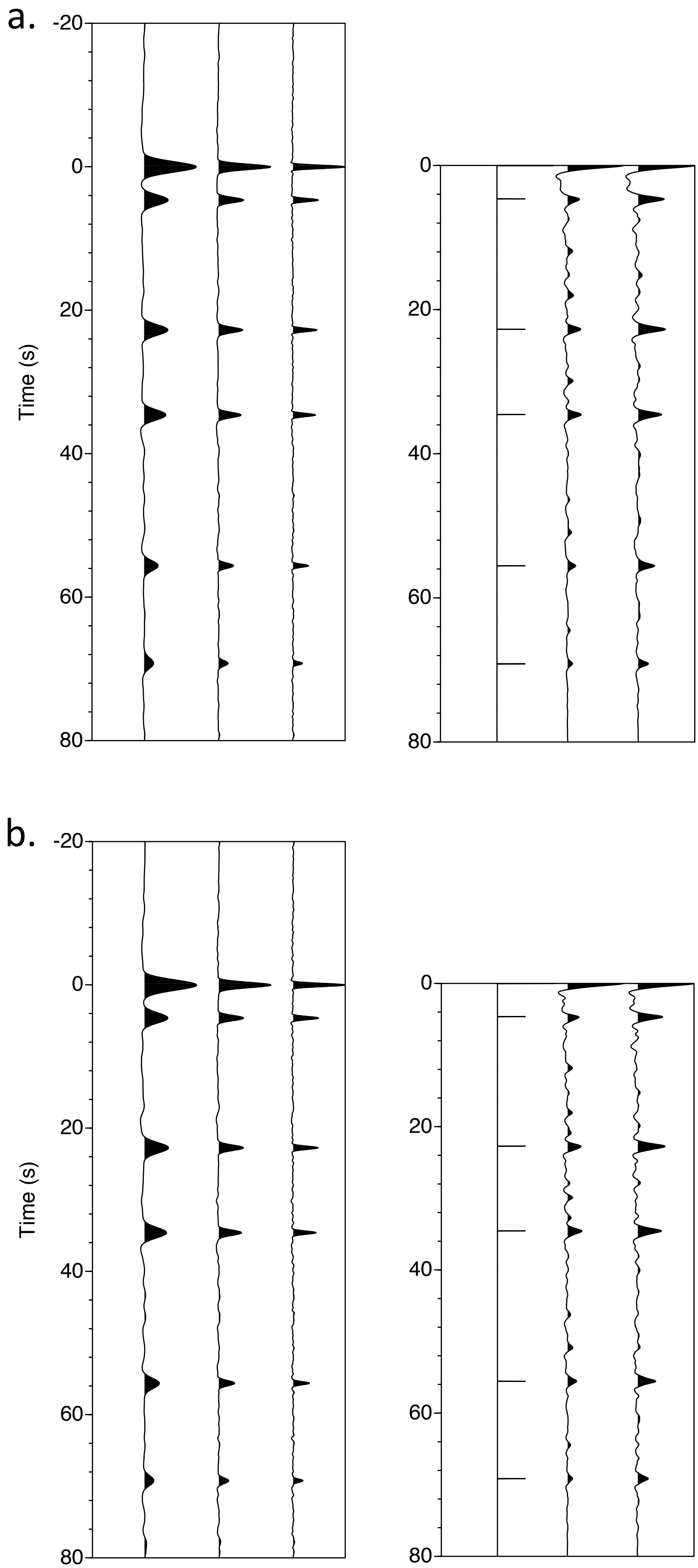
a.
-20
0
20
40
60
80
Time (s)
0
20
40
60
80
b.
-20
0
20
40
60
80
Time (s)
0
20
40
60
80

Figure S7

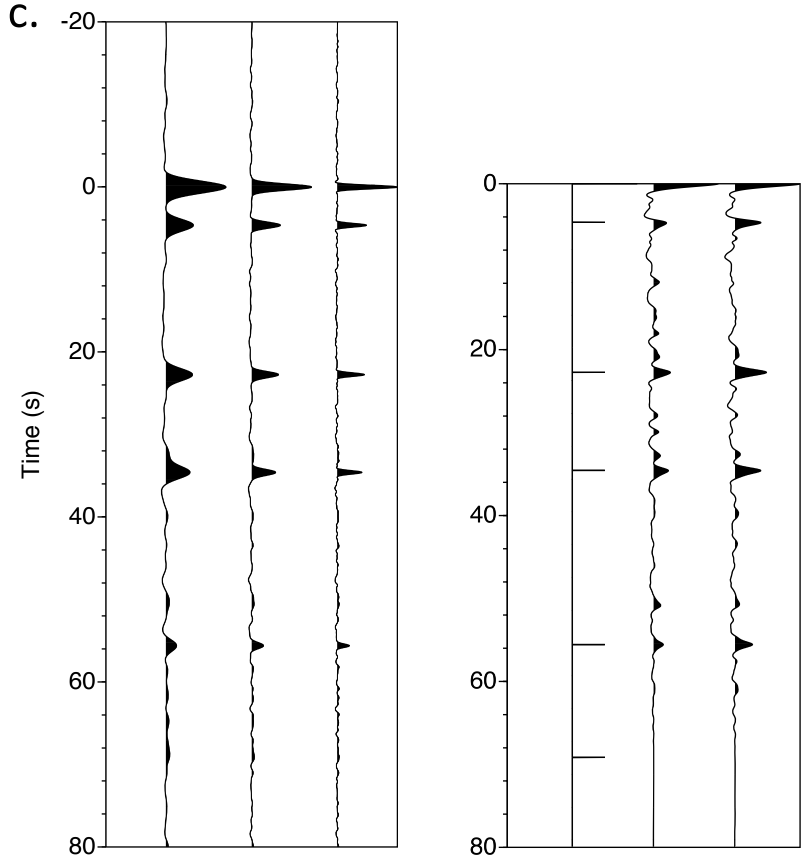

Figure S7

Figure S7. Stacking of filtered traces for multiple earthquakes. Synthetic traces were generated for all the events listed in Table S1, beginning with the effective source wavelets derived by stacking waveforms for stations deployed north of the Atlantic Coastal Plain, then proceeding as described for Figure S6. Left panel: stack of deconvolved traces for a range of Gaussian smoothing parameters (α=1, 2, 4). Right panel, first trace: the 6 impulses used to generate the synthetic seismograms; second trace: stack of the zero and positive lags of the autocorrelations of the synthetic seismograms; and third trace: stack of the zero and positive lags of the cross correlations of the synthetic seismograms with the effective source wavelets. Stacking suppresses artifacts in the deconvolved traces but some of the sidelobe energy in the correlated traces remains.

a. Stacks of waveforms for the 16 earthquakes used to generate the output sections shown in Figures 2, 4, S2, and S5 (events 1-16 in Table S1). All reflections are recovered but the two latest reflections are attenuated.

b. Stacks of waveforms for the 8 earthquakes used to generate the output section shown in Figure S3 (events 1-3; 8, 10, 11, 13, 14 in Table S1). Again, all reflections are recovered but the two latest reflections are attenuated.

c. Stacks of waveforms for the 6 earthquakes used to generate the output sections shown in Figures 3 and S4 (events 1, 2, 8, 10, 11, 14 in Table S1). The latest reflection is not recovered because of the shorter listening window (70 s) used for these earthquakes rather than 80 s as used for most of the earthquakes in Figures S7a and S7b).

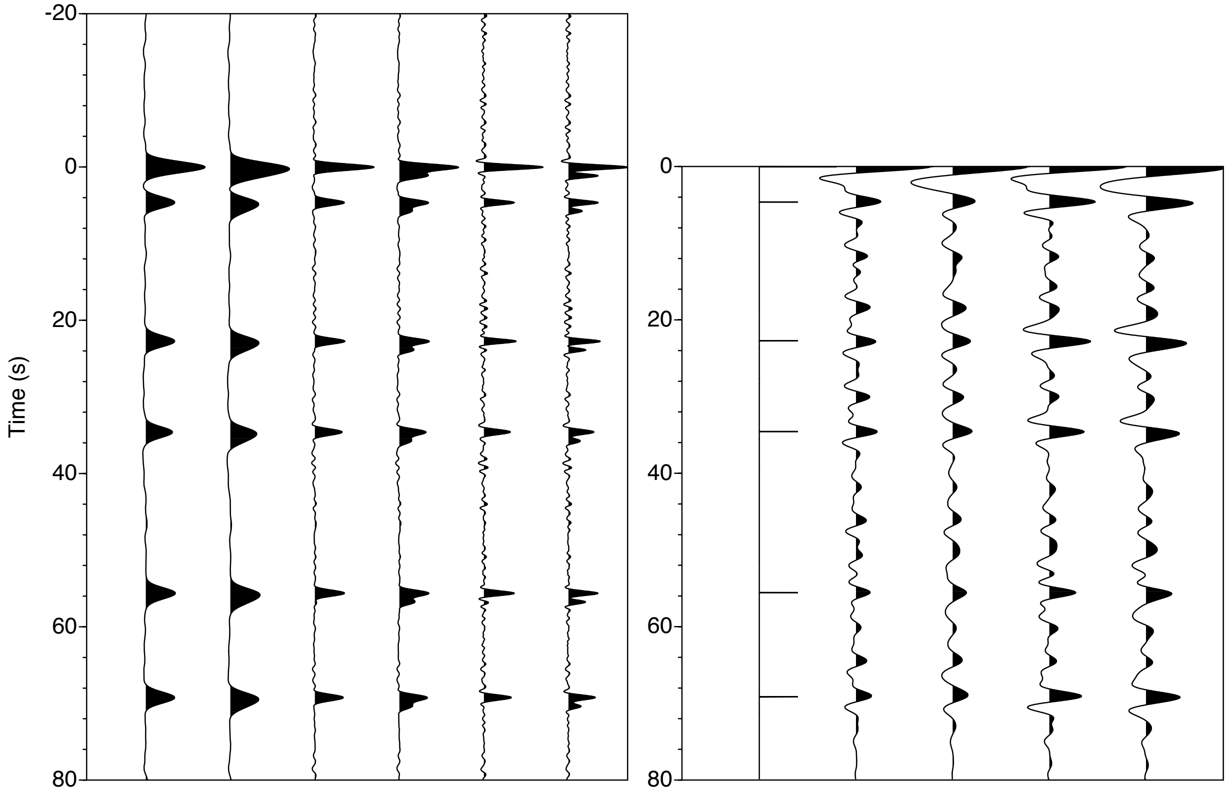

Figure S8.

Figure S8. Comparison of deconvolution, autocorrelation, and cross-correlation for long-duration effective source wavelets. Similar to Figure S6, except for the addition of a second input seismogram (second trace for each pair of traces) generated using a source wavelet that is now the sum of the original source wavelet for event 13 (Table S1) and the same wavelet delayed by 1.1 s, to simulate the effect of differential moveout for PKPdf and PKiKP between stations north of the Coastal Plain and the southernmost station in Line E. The amplitude of the PKiKP contribution is assumed to be half that of the PKPdf contribution, and for simplicity, the phase angle is assumed to be the same.

The left panel shows the synthetic seismograms deconvolved in the frequency domain by the original source wavelet using a water-level of 0.001 and a range of Gaussian smoothing parameters (α = 1, 2, 4). The beginning and end of traces were linearly tapered over a window of 3 s prior to Fourier transformation. Each pair of traces shows reflections for coincident PKPdf/PKiKP arrivals (first trace of each pair) and the two arrivals separated by 1.1 s (second trace of each pair), for a given value of α. As expected, differential moveout generates additional cycles for each reflection.

The righthand panel shows the 6 impulses (first trace) used to generate the synthetic seismograms, the zero and positive lags of the autocorrelation of the synthetic seismogram for coincident PKPdf and PKiKP (second trace), the autocorrelation for PKPdf and PKiKP separated by 1.1 s (third trace), and zero and positive lags of the cross correlation of the synthetic seismograms with the original source wavelet, again for coincident PKPdf and PKiKP (fourth trace) and the two arrivals separated by 1.1 s (fifth trace). Differential moveout generates a slight broadening of the waveform, accompanied by a small delay for the cross-correlated waveforms.

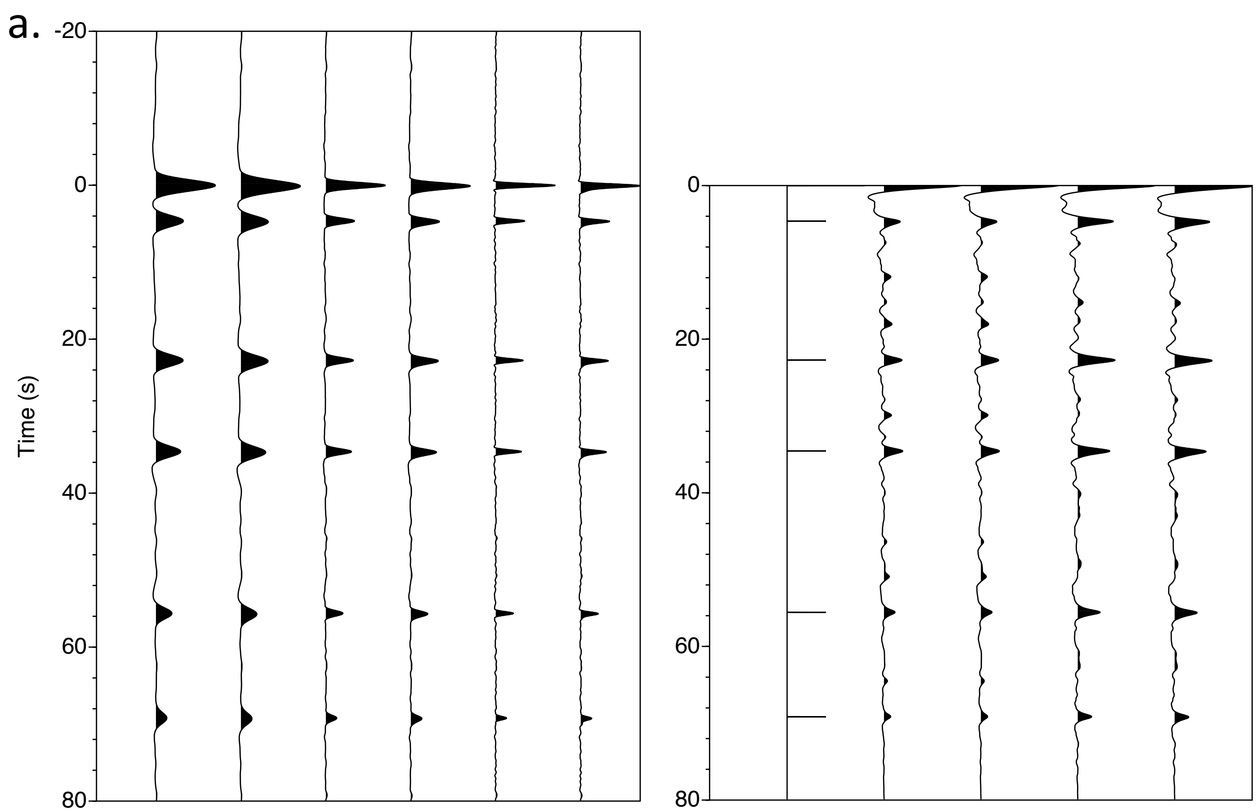

Figure S9

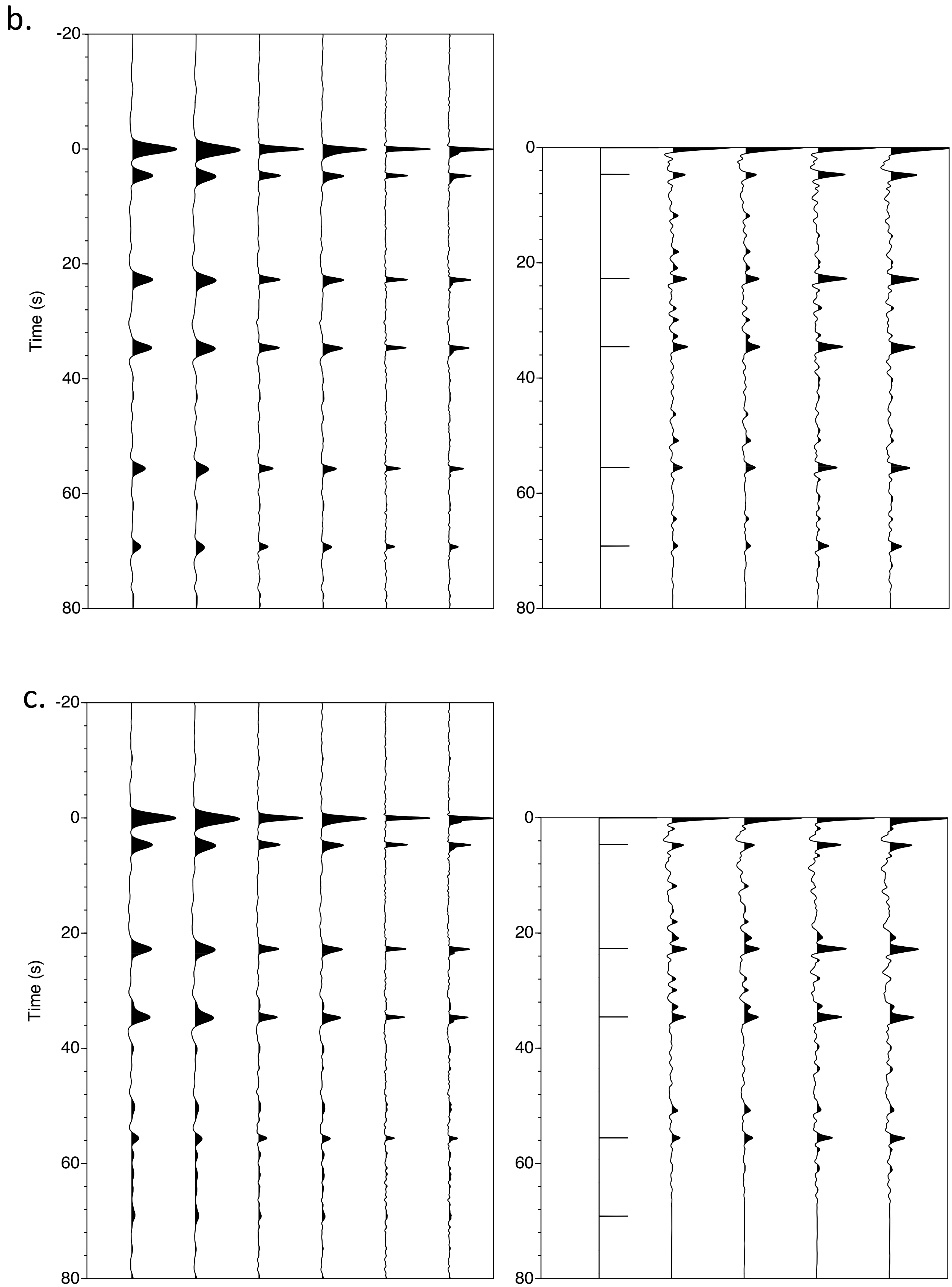

Figure S9

Figure S9. Similar to Figure S8, except that filtered traces have been stacked for multiple earthquakes. Deconvolution and cross correlation were carried out using the source wavelet derived for each event (Table S1).

The lefthand panel shows stacks of synthetic seismograms deconvolved in the frequency domain by the original source wavelet for each earthquake, using a water-level of 0.001 and a range of Gaussian smoothing parameters (α = 1, 2, 4). Each pair of traces shows reflections for coincident PKPdf/PKiKP arrivals (first trace of each pair) and the two arrivals separated by 1.1 s (second trace of each pair), for a given value of α.

The righthand panel shows the 6 impulses (first trace) used to generate the synthetic seismograms, stacks of the zero and positive lags of the autocorrelations of the synthetic seismograms for coincident PKPdf and PKiKP (second trace), stacks of the autocorrelations for PKPdf and PKiKP separated by 1.1 s (third trace), and stacks of the zero and positive lags of the cross correlations of the synthetic seismograms with the original source wavelets, again for coincident PKPdf and PKiKP (fourth trace) and the two arrivals separated by 1.1 s (fifth trace).

a. Stacks of waveforms for the 16 earthquakes used to generate the output sections shown in Figures 2, 4, S2, and S5 (events 1-16 in Table S1). Stacking compresses wavelets broadened by differential moveout.

b. Stacks of waveforms for 7 of the 8 earthquakes used to generate the output section shown in Figure S3 (events 1-3; 8, 10, 11, 13 in Table S1; event 14 was not recorded at the southernmost station). In the stack of the deconvolved traces (left panel), wavelets are compressed but some of the wavelet asymmetry remains. In the stack of the cross correlated traces (right panel), wavelets still show a small delay.

c. Stacks of waveforms for 5 of the 6 earthquakes used to generate the output sections shown in Figures 3 and S4 (events 1, 2, 8, 10, 11, in Table S1; again, event 14 was not recorded at the southernmost station). As in Figure S9b, some of the wavelet asymmetry and delay remains.

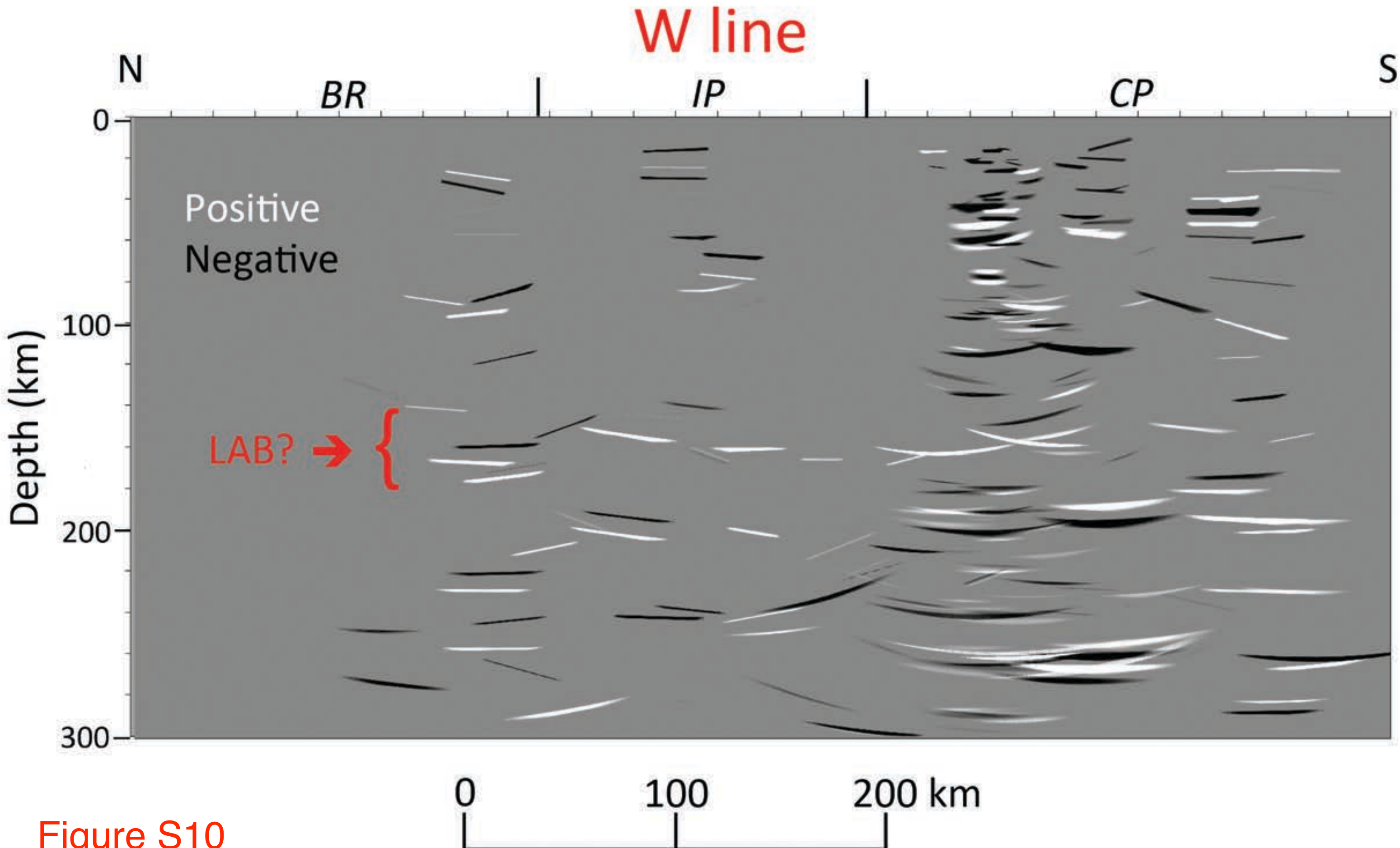
W line
N
S
BR
IP
CP
Positive
Negative
LAB?
Depth (km)
0
100
200
300
0
100
200 km

Figure S10

Figure S10. Preliminary migrated section for Line W, showing reflections identified in coherency-filtered slant stacks of small-aperture gathers extracted for events 1, 2, 3, 4, 7, 11, 13, and 16 (Table S1). White: reflections from positive impedance contrasts; black: reflections from negative impedance contrasts.

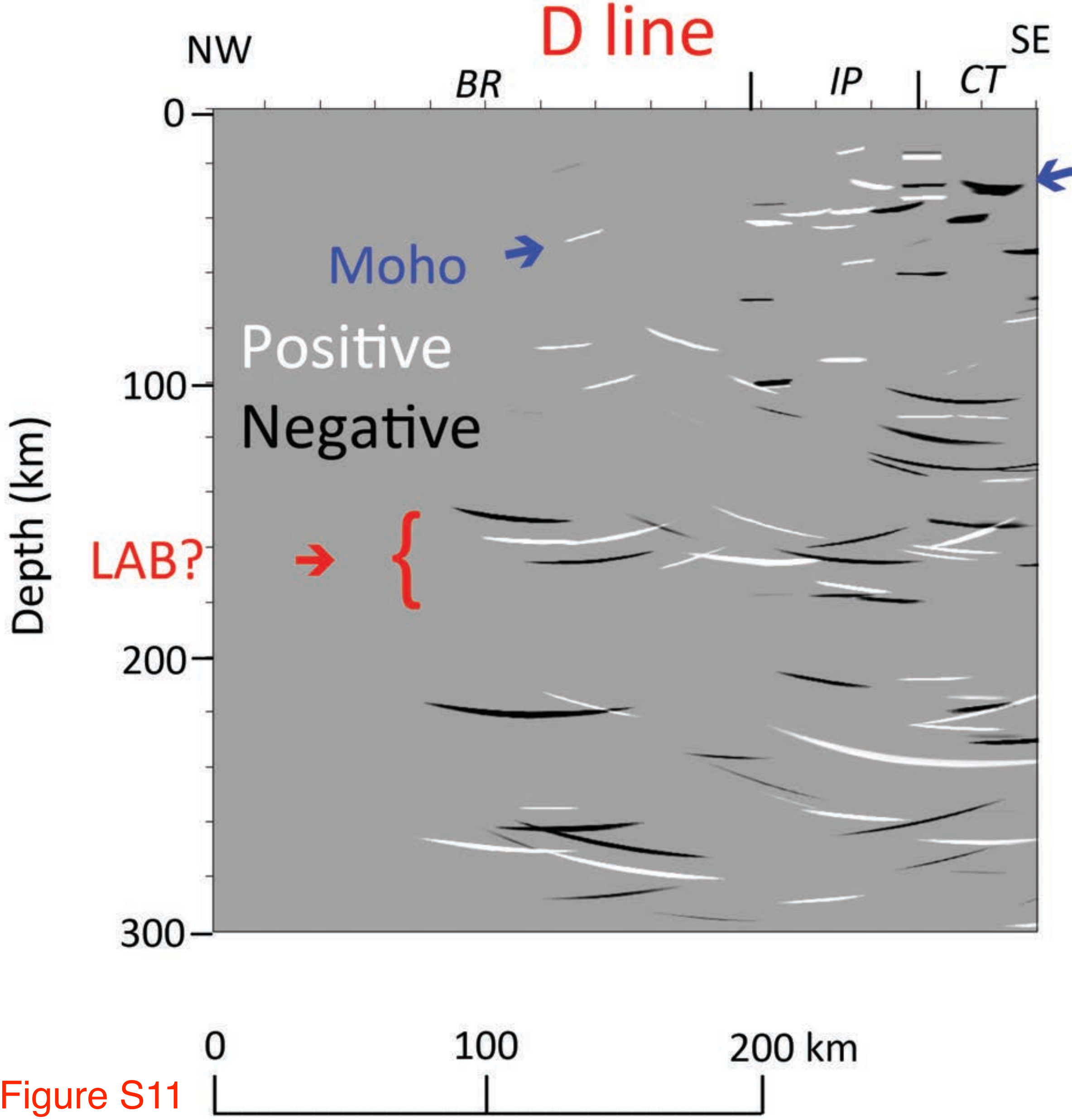
D line
NW
SE
BR
IP
CT
Moho
Positive
Negative
LAB?
Depth (km)
0
100
200
300
0
100
200 km

Figure S11

Figure S11. Preliminary migrated section for Line D, showing reflections identified in coherency-filtered slant stacks of small-aperture gathers extracted for events 1, 3, 4, 7, 11, 13, and 16 (Table S1). White: reflections from positive impedance contrasts; black: reflections from negative impedance contrasts.

Table S1. Earthquakes used for analysis of PKIKP phases [1, 2, 3].							
Event #	Date & Time (UT)	Lat. (°N)	Long (°E)	Depth (km)	Magnitude (Mw)	Back-Azimuth (°)	Distance (°)
1	2013-07-07 18:35:31.38	-3.92	153.92	386.3	7.3	D: 286.2-286.7 W: 286.3-283.8 E: 286.5-284.4	117.8-120.0 118.3-119.6 120.4-121.4
2	2014-04-11 07:07:22.81	-6.59	155.05	60.5	7.1	D: 283.0-283.4 W: 283.1-280.5 E: 283.1-281.2	118.5-120.6 119.0-120.0 121.0-121.8
3	2013-07-07 20:30:07.38	-6.02	149.72	62.0	6.6	D: 287.3-287.8 W: 287.4-284.4 E: 287.4-284.9	122.4-124.6 122.9-124.2 125.0-126.1
4	2012-04-17 07:13:49.88	-5.53	147.13	208.2	6.9	D: 289.9-290.1 W: 289.8-286.6	125.3-126.4 124.6-126.1
5	2011-07-31 23:38:58.09	-3.51	144.97	19.6	6.6	D: 293.5-293.8 W: 293.3-290.2	125.5-126.8 125.0-126.8
6	2012-03-21 22:15:05.59	-6.22	146.0	117.7	6.6	D: 290.1-290.3 W: 290.0-286.6	126.4-127.7 125.9-127.4
7	2011-12-14 05:04:57.81	-7.53	146.81	128.5	7.1	D: 288.2-288.4 W: 288.1-284.7	126.6-127.8 126.1-127.5
8	2012-08-31 12:47:35:54	10.81	126.83	44.4	7.6	D: 321.3-322.7 W: 321.6-319.3 E: 322.6-320.7	125.3-127.9 125.9-129.6 128.4-131.4
9	2012-02-06 03:49:13.92	9.92	123.22	17.5	6.7	D: 325.3-326.2 W: 324.9-322.6	129.0-130.4 128.5-132.3
10	2013-10-15 00:12:33.25	9.83	124.12	23.2	7.1	D: 323.6-325.1 W: 323.9-321.5 E: 325.0-323.0	127.5-130.0 128.1-131.9 130.6-133.7
11	2013-04-06 04:42:36.19	-3.51	138.48	66.0	7.0	D: 298.7-299.3 W: 298.8-295.5 E: 299.0-295.1	129.2-131.6 129.8-131.8 132.1-133.8
12	2012-04-21 01:16:53.67	-1.69	134.32	24.4	6.7	D: 304.6-305.0 W: 304.4-300.7	131.9-133.3 131.4-134.0
13	2012-10-17 04:42:31.06	4.18	124.56	338.4	6.0	D: 319.3-320.7 W: 319.6-316.5 E: 320.5-318.0	132.1-134.7 132.7-136.3 135.2-138.1
14	2012-08-26 15:05:37.16	2.19	126.84	91.1	6.6	D: 315.3-316.5 W: 315.5-312.5 E: 316.3-314.6	132.5-135.0 133.1-136.2 135.6-137.2
15	2011-06-13 14:31:23.40	2.54	126.46	66.0	6.4	D: 316.6-317.2 W: 316.2-312.9	133.6-135.0 133.0-136.4
16	2011-12-13 07:52:12.03	0.05	123.06	167.4	6.1	D: 318.6-319.4 W: 318.3-314.6	137.5-138.9 137.0-140.5

[1]All 16 events were used for the stacks in Figures 2, 4, S2, and S5
[2] Events 1, 2, 3, 8, 10, 11, 13, 14 were used for the stacks in Figure S3
[3] Events 1, 2, 8, 10, 11, 14 were used for the stacks in Figures 3 and S4

Table S1.

Title: “Table S1. Earthquakes used for analysis of PKIKP phases”

Contents: This table summarizes parameters for the 16 earthquakes used for the paper.

Column 1: Event numbering roughly in order of increasing epicentral distance.

Column 2: “Date”: date of the earthquake listed as year-month-day; “Time”: Universal time of the earthquake.

Column 3: “Lat. (°N)”: latitude of the epicenter in degrees north of the equator

Column 4: “Long. (°E): longitude of the epicenter in degrees east of the prime meridian.

Column 5: “Depth (km)”: depth of the earthquake focus in kilometers.

Column 6: “Magnitude (Mw)”: moment magnitude of the earthquake.

Column 7: “Back-Azimuth (°): the range in back-azimuth in degrees clockwise from north from SESAME stations to the epicenter. “E”, W”, and “D” refer to back-azimuths for stations along the N-S striking Eastern line, the N-S striking Western line, and the NW-striking line, respectively (Figure 1).

Column 8: “Distance (°): the range in angular distance between the stations and epicenter.